# Experimental investigation of bubble dynamics and flow patterns during flow boiling in high aspect ratio microchannels with the effect of flow orientation

Arif Widyatama [a,b], Mandi Venter [a,c], Daniel Orejon [a], Khellil Sefiane [a,*]

[a] *Institute for Multiscale Thermofluids, School of Engineering, University of Edinburgh, The King's Buildings, Edinburgh, EH9 3FD, UK*
[b] *Department of Mechanical & Industrial Engineering, Faculty of Engineering, Universitas Gadjah Mada, Jalan Grafika No.2, Yogyakarta, 55281, Indonesia*
[c] *Faculty of Engineering, University of Pretoria, Lynnwood Road, Hatfield, 0028, Pretoria, SA, South Africa*

ABSTRACT

Multiphase flow and boiling phase-change within microchannels are of paramount importance to thermal management and electronics cooling, among others. The present experimental study investigated the bubble dynamics and flow patterns during flow boiling in a high aspect ratio microchannel at different channel orientations. Hydrofluoroether (HFE−7000) was used as the working fluid within a transparent glass microchannel with a width-to-height aspect ratio of 10 and a hydraulic diameter of 909 μm. A tantalum layer coating was applied to the channel, allowing visual observation to be conducted whilst imposing uniform heating along the channel. Under horizontal and vertical upward flow, the mass fluxes were varied between 14 kg m$^{-2}$ s$^{-1}$ and 42 kg m$^{-2}$ s$^{-1}$ for Reynolds numbers between 28.4 and 85.2, while the heat fluxes were set from 2.8 kW m$^{-2}$ to 18.7 kW m$^{-2}$. The results show that single bubble growth can be divided into three stages, namely: bubble-free growth, partially confined bubble growth, and fully confined growth. The effects of mass flux and heat flux on bubble behaviour and transition points between the defined stages are discussed. Equally important, the channel orientation influences the bubble behaviour in terms of bubble evolution, bubble shape, and bubble nose velocity, with no significant differences observed for the flow patterns when comparing horizontal and vertical upward cases. The comparison of the present work with previous flow pattern map results from the literature shows that earlier flow pattern transition models cannot accurately predict the observed flow patterns in the present configuration. Two types of instabilities are observed, which are associated with the dominant flow pattern during flow boiling and hence a function of the mass flux to heat flux ratio. The first type of instability, high amplitude and long period oscillation, is found during slug flow which is characterised by the presence of bubble rapid expansion along the channel. In addition, a second instability ensues when churn and annular flow create short period oscillations due to the high number of nucleation events, bubble coalescence, and the breakage of liquid slug or liquid film.

## 1. Introduction

The rapid miniaturisation and/or increase in power of microelectronic devices and the wide application of compact refrigeration systems in the last decades have created an urgent need to have a reliable thermal management system that can handle high heat flux dissipation while maintaining the device high performance. A promising solution that is receiving attention to address this issue is the utilisation of flow boiling phase-change in microscale heat exchangers, which consists of single or multiple microchannels. Flow boiling is an enhanced heat transfer mechanism when compared to single-phase liquid cooling due to larger thermal energy that can be removed and then dissipated by the latent heat of vaporization as opposed to single-phase systems merely relying on sensible heat [1]. In addition, with the appropriate working fluid selected, boiling phase-change can operate at nearly isothermal conditions [2]. This can prevent temperature variations, which become the main source of thermo-mechanical fatigue, wear-out and/or burnout leading to the device failure [3]. To this end, microchannel flow boiling is advantageous as increased heat fluxes can be dissipated under relatively low mass flow rates resulting in reduced system pumping power requirements due to smaller pressure drops, whilst in the case of

## Nomenclature

### Roman Letters

| | |
|---|---|
| $A$ | Area [mm$^2$] |
| $Bo$ | Boiling number, $\frac{q}{Gh_{fg}}$ [$-$] |
| $Bd$ | Bond number, $\frac{g(\rho_l - \rho_v)D_h^2}{\sigma}$ [$-$] |
| $Co$ | Confinement number, $\sqrt{\frac{\sigma}{g(\rho_l - \rho_v)D_h^2}}$ [$-$] |
| $CF$ | Calibration factor [mm pix$^{-1}$] |
| $C_p$ | Specific heat capacity [J kg$^{-1}$ K] |
| $D$ | Diameter [mm] |
| $D_h$ | Hydraulic diameter [mm] |
| $d$ | Thickness [mm] |
| $F$ | Force [N] |
| $G$ | Mass flux [kg m$^{-2}$ s$^{-1}$] |
| $g$ | Gravitational acceleration [m s$^{-2}$] |
| $h$ | Heat transfer coefficient [W m$^{-2}$ K$^{-1}$] |
| $H$ | Depth [mm] |
| $I$ | Current [A] |
| $k$ | Thermal Conductivity [W m$^{-1}$ K$^{-1}$] |
| $L$ | Length [mm] |
| $\dot{m}$ | Mass flow rate [kg s$^{-1}$] |
| $P$ | Pressure [mbar] |
| $Q$ | Heat [W] |
| $q$ | Heat flux [W m$^{-2}$] |
| $Re$ | Reynolds number, $\frac{\rho V D_h}{\mu}$ [$-$] |
| $Su$ | Suratman number, $\frac{\rho \sigma D}{\mu^2}$ [$-$] |
| $T$ | Temperature [°C] |
| $t$ | Time [ms] |
| $U$ | Voltage [V] |
| $\dot{V}$ | Volumetric flow rate of the pump [m$^3$ s$^{-1}$] |
| $v$ | Flow velocity [m s$^{-1}$] |
| $V$ | Volume [m$^3$] |
| $W$ | Width [mm] |
| $We$ | Weber number, $\frac{G^2 D}{\sigma \rho}$ [$-$] |
| $We^*$ | Modified Weber number [$-$] |
| $X$ | Vapour quality [$-$] |
| $X_{tt}$ | Lockhart–Martinelli parameter turbulent liquid-turbulent vapour flows, [$-$] |
| $z$ | Distance from the inlet, measured in axis parallel to channel length [mm] |

### Greek Letters

| | |
|---|---|
| $\alpha$ | Channel aspect ratio [$-$] |
| $\beta$ | Bubble length-to-width aspect ratio [$-$] |
| $\varepsilon$ | Channel emissivity [$-$] |
| $\varphi$ | Heat transfer efficiency [$-$] |
| $\mu$ | Dynamic Viscosity [kg m$^{-1}$ s$^{-1}$] |
| $\pi$ | Pi constant [$-$] |
| $\rho$ | Density [kg m$^{-3}$] |
| $\sigma$ | Surface tension [N/m] |
| $\omega$ | Stefan–Boltzmann constant [W m$^{-2}$ K$^{-4}$] |

### Subscripts

| | |
|---|---|
| A | Annular region |
| amb | Ambient condition |
| B | Bubble |
| b | Buoyancy |
| c | The cross-sectional area of the channel |
| CB | Coalescing bubble region |
| ch | Channel |
| conv | Losses due to convection |
| Eff | Effective |
| G | Gas/Vapour phase condition |
| In | Inlet condition, the inner surface |
| IB | Isolated bubble region |
| input | Input |
| L | Liquid phase condition |
| loss | Losses |
| mm | Parameter measured in mm |
| out | Outlet condition, the outer surface |
| pix | Parameter measured in pixel |
| rad | Losses due to radiation |
| sp | Single phase |
| SL | Liquid superficial |
| SG | Gas/vapour superficial |
| tp | Two-phase |
| w | Wall condition |

single-phase cooling, larger flow rates are often needed [4].

When looking into the different parameters or conditions influencing flow boiling, as mentioned in Refs. [5–7], channel geometry is considered an important factor. Different shapes and aspect ratios of these channels, including circular tubes [8–10], rectangular ducts, and other specific geometries such as a trapezoidal microchannel [11] and diverging microchannels [12], have been reported in the literature. For a rectangular geometry, channels with a high width-to-height aspect ratio have received special attention due to their large surface-to-cross-sectional area ratio, which eventually minimises the working fluid flow rates [13] whilst enabling increased heat transfer [14]. Besides increasing the surface-to-cross-sectional area in these high aspect ratio channels, equally important is the heat transfer mechanism dictated by the bubble behaviour, which can be divided into two stages namely partial bubble confinement (dictated by channel depth) and full bubble confinement (dictated by channel width). These confinement stages are intrinsic to high aspect ratio channels and are not found in circular or low aspect ratio rectangular ones.

Another important parameter in flow boiling is the channel orientation. This can be achieved by azimuthal rotation, i.e., the rotation axis is in the same direction as the fluid flow [15] and/or by inclination [16]. In terms of heat transfer performance, many studies have demonstrated that vertical downward flow produced the lowest heat transfer coefficients. This trend was found to be associated with the increased flow reversal present due to buoyancy force, which restricts the bubble movement towards the channel outlet [16]. In contrast, previous studies have provided contrasting views on the effect of channel inclination on best heat transfer performance. An investigation of flow boiling of R245fa within a 3 mm circular channel was conducted by Bamarovat Abadi et al. [17], and the results showed that vertical upward flow configurations resulted in the highest heat transfer coefficients. In the study of flow boiling of R245fa in a 1.6 mm circular channel conducted by Laysaac et al. [18], it was concluded that there was no strong correlation between the channel orientation and the heat transfer performance. In addition, Piasecka et al. [19] investigated flow boiling of FC-72 in a 1.7 mm depth single bottom-heated channel for horizontal and vertical flow cases. At low heat fluxes, horizontal flow showed the highest heat transfer coefficient, whilst vertical upward flow performed better at high heat fluxes. In the same line of work, the research conducted by Sinha and Srivastava [20] revealed that for low Reynolds numbers, vertical upward flow showed better performance in terms of evaporative heat flux when compared to vertical downward flow, whilst for high Reynolds numbers, such differences in the heat transfer performance were not significant.

In addition to studies focusing on heat transfer, the works conducted by Kandlikar and Balasubramanian [21] and by Zhang and Pinjala [22] suggested that channel inclination also influenced pressure drop characteristics. This was ascribed to buoyancy forces working in the same direction as the mass flow during upward flow, aiding bubble movement inside the microchannel. More specifically, Leão et al. [23] studied the flow boiling of R245fa in a rectangular microchannel heat sink ($D_H = 0.2$ mm and aspect ratio of 0.5) and concluded that vertical upward flow configuration reduced the occurrence of flow reversal. In a different flow boiling study using water in a rectangular microchannel with a hydraulic diameter of 0.94 mm, Li et al. [24] observed that at low mass fluxes, the highest total pressure drop was found in the vertical downward flow configuration. In contrast, a further increase in the mass flux caused the horizontal flow to produce the highest pressure drop due to the dominance of inertial flow. Some other studies providing analysis and discussion on flow pattern characteristics for channels at different orientations pointed out that different channel orientations may influence the flow characteristics, such as the presence of a more pronounced flow reversal [21,25], and/or the change of flow transition patterns [17, 26]. In view of the above, there is still a lack of understanding of the effect of channel orientation on the flow boiling mechanisms within high aspect ratio microchannels, which highlights the importance of this investigation.

Hence, the analysis of bubble dynamics plays an important role in understanding the heat transfer performance during microchannel flow boiling. The presence of bubble nucleation followed by growth and departure is suggested to enhance the heat transfer performance [27, 28]. More specifically, the flow boiling mechanistic model proposed by Thome et al. [29], and later adopted by Wang et al. [30] for the rectangular microchannel case, considered the importance of the thin liquid film between the elongated bubble and the channel wall in the heat transfer process. While a thin liquid film is beneficial, its control results rather challenging, which can lead to dry-out phenomena and the formation of annular flow, which are responsible for the drop in heat transfer performance [31–33]. In order to better elucidate quantitively the parameters such as bubble dynamics, liquid film thickness and/or bubble-wall interaction, the use of various non-intrusive approaches have been proposed, such as shadowgraphy [34], a combination of shadowgraphy and impedance-based sensing [35], Schlieren visualisation [36], and optical probing [37]. These investigations and accurate quantification techniques and information are crucial for microscale applications, which are very sensitive to any disturbance inside the channel.

When looking into the bubble dynamics, bubble confinement imposes unique characteristics that distinguish two-phase flow at the micro-scale from that seen in more conventional macro-scale systems. Although the behaviour in the early stage can be approached to bubble growth under pool boiling conditions, the confinement caused by channel depth influences the bubble dynamics in several ways, such as the rapid increase of bubble growth rate [38] and periodic bubble deformation [39]. Further description of the criteria of bubble confinement has been discussed by Yin and Jia [39], who observed the bubble height-to-width ratio to define the transition between the free growth stage and the confined growth stage. The confinement effect can affect the general flow characteristics, as demonstrated by Gedupudi et al. [40], who considered bubble confinement events during the model development of bubble growth associated with pressure drop along the channel. Equally important, in the presence of a rectangular channel, a bubble experiences two stages of confinement affected by channel geometry, namely partial confinement and full confinement. As suggested by Barber et al. [41], the transition between those confinement stages caused pressure fluctuations along the channel. Hence, further investigation should be carried out to reveal the bubble behaviour in the rectangular channel, especially with a high aspect ratio where the confinement effect from the channel depth and width takes place in a different time scale.

Several predictions of the dominant flow patterns for microchannel flow boiling at particular conditions have been achieved by developing two-phase flow pattern maps. To this end, Akbar et al. [42], using various databases of air-water flow, proposed a flow pattern map with the Webber number for liquid and gas phases in the axis coordinates for vertical and horizontal configurations. Harirchian and Garimella [43, 44] suggested that confinement characteristics also affected flow patterns during microchannel flow boiling. They produced a flow pattern map and proposed the convective confinement number, which is a function of the Bond number and Reynolds number, to act as the transition line between the confined slug and bubbly flow. Although numerous flow pattern maps have been proposed, their validity is limited to specific conditions concerning channel geometry, operating conditions, and working fluid selection. Mahmoud and Karayiannis [45] attributed the lack of agreement between proposed flow pattern maps to the uncertainty about which parameters govern the domination and development of flow patterns. In addition, different flow pattern definitions result in added complexity when attempting to combine experimental findings to develop a universal flow pattern map.

As reviewed above, the present study addresses systematically the effect of confinement and, more importantly, the bubble elongation dynamics, as well as bubble transitions and regimes, building up on earlier works where only bubble growth before the onset of elongation was reported. In addition, the present study tackles the bubble behaviour on these high aspect ratio microchannels in horizontal and vertical upward flow where buoyancy plays a major role in the flow characteristics. Last, flow pattern and instability regime maps specific to this configuration are provided as these were not predicted accurately by earlier methods and proposed regimes in the literature. To achieve the present study's aims and objective, a single rectangular microchannel with a hydraulic diameter of 909 μm and a high width-to-height aspect ratio of 10, supported with transparent uniform heating method, was utilised. In the present work, we first explain the single bubble during flow boiling of HFE−7000 in terms of bubble growth stages and the transition criteria. Next, the effect of mass flux, heat flux, and flow orientation on bubble behaviour are discussed. Equally important, the observed flow pattern during flow boiling is analysed and compared to previously proposed transition lines of flow pattern. The flow instability is lastly examined by analysing the flow visualisation supported by pressure and temperature fluctuation during flow boiling.

## 2. Experimental methodology

### 2.1. Research equipment

The research was conducted within an in-house built experimental facility located in the two-phase flow heat transfer laboratory at The University of Edinburgh. The facility had been used in multiple previous studies [13,15]. However, some adjustments were made to accommodate the objectives of the present study. Fig. 1 presents a schematic of the main components required to achieve, observe, record and analyse flow boiling within the single-pass flow path. These components included a syringe pump, heating system, test section, reservoir, high-speed video camera, infrared (IR) thermal camera, DAQ system, and temperature and pressure measurement devices.

Hydrofluoroether HFE−7000 ($C_3F_7OCH_3$) or Novec 7000 from 3M$^{TM}$ was utilised as the working fluid. The liquid is non-corrosive, non-flammable, and has excellent dielectric properties suitable for various heat transfer applications [46]. The relatively low saturation temperature, 34 °C at 1 atm, is lower than most electronic component's upper operating threshold and requires lower heat fluxes to achieve boiling incipience. Some main thermophysical properties of Novec 7000 are listed in Table 1.

The working fluid was supplied to the test section via a Cole-Parmer syringe pump (series 100, USA). A 50 ml Fortuna glass syringe with an inner diameter of 26.9 mm was used and specified on the pump settings
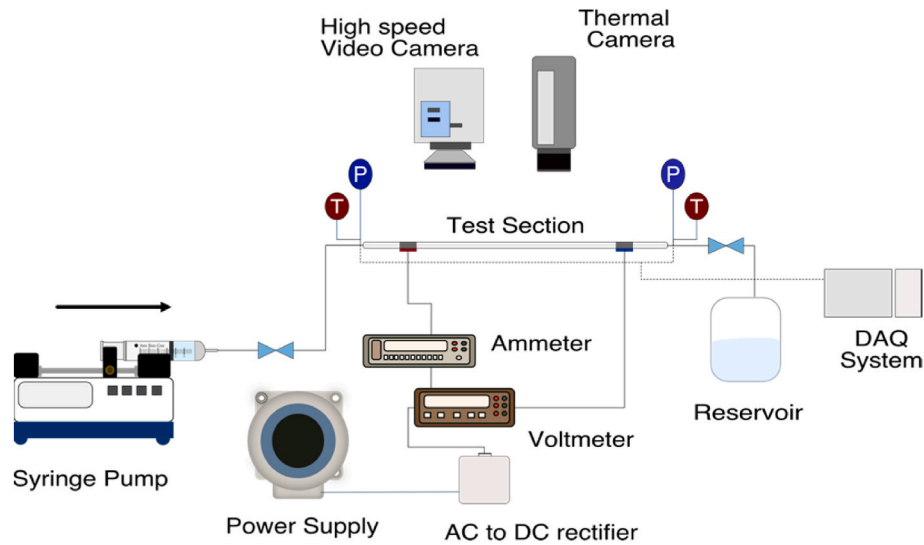
**Fig. 1.** Schematic of the experimental setup. In general, it consists of a syringe pump, heating system, test section, high-speed video camera, infrared (IR) thermal camera, temperature and pressure measurement devices, DAQ system, and reservoir.

**Table 1**
Physical properties of Novec 7000 (25 °C, 1 atm) [46].

| Properties | Unit | Value |
|---|---|---|
| Boiling point ($T_{sat}$) | °C | 34 |
| Liquid density ($\rho_l$) | kg m$^{-3}$ | 1400 |
| Liquid specific heat ($C_p$) | J kg$^{-1}$ K$^{-1}$ | 1300 |
| Liquid thermal conductivity ($k$) | W m$^{-1}$ K$^{-1}$ | 0.075 |
| Latent heat of vaporization ($h_{fg}$) | kJ kg$^{-1}$ | 142 |
| Surface tension ($\sigma$) | N m$^{-1}$ | 0.0124 |
| Kinematic viscosity ($\nu$) | cSt | 0.32 |
| Vapour pressure ($P$) | Pa | 64.6 |

before operation. By specifying the custom syringe size, the pump could convert the axial displacement of the pusher block (caused by the stepper motor and screw movement) to the desired liquid volume flow rate. In addition, either the target pumping duration or the target injected volume could be specified.

A combination of flexible and rigid tubing, together with push-pull fittings, were used to create the flow path connecting the test section to both the syringe pump and the reservoir. A rectangular borosilicate glass channel was used as the test section while short circular tubes were glass blown onto the ends of the channel towards successfully installing the rectangular microchannel into the flow path and easing fluid transportation. As presented in Fig. 2, the channel had a length ($L$) of

100 mm, an inner width ($W_{in}$) of 5 mm, an inner depth ($H_{in}$) of 0.5 mm and a wall thickness ($d$) of 0.35 mm. Hence, it had a width-to-height aspect ratio ($\frac{W_{in}}{H_{in}}$) of 10 and a hydraulic diameter, calculated by equation (1) of 909 µm.

$$D_h = \frac{2W_{in}H_{in}}{W_{in} + H_{in}} \tag{1}$$

Of importance to this work and to the bubble characteristic is the estimation of the dimensionless confinement number ($Co$) proposed by Kew and Cornell [47], which is determined by the following equation.

$$Co = \sqrt{\frac{\sigma}{g(\rho_l - \rho_v)D_h^2}} \tag{2}$$

The confinement number was associated with the restriction of a channel to the normal flow regime for a specific working fluid. It was suggested that when $Co > 0.5$, the confinement effect would be significant and hence confined bubble regime is dominant which can be used as the transition criteria from macro to microscale [6]. The confinement number for this specific channel geometry and working fluid case was $Co = 1.05$, which was higher than the critical value. Hence it can be classified as a microchannel. It should be noted that other channel classifications can be further useful allowing for better comparison with other works in the literature. For instance, Kandlikar and Grande [48], based on the rarefaction effect on gas flow, proposed the channel
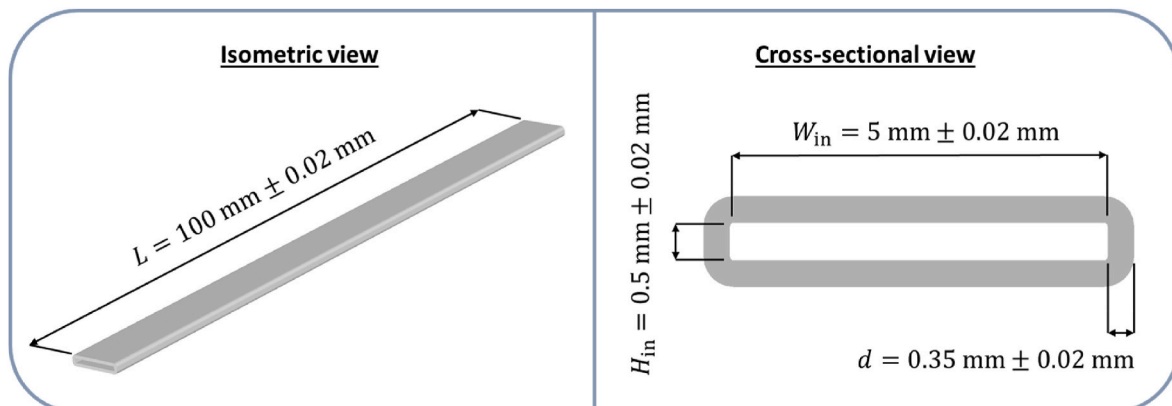


**Fig. 2.** Schematic showing (left) an isometric and (right) cross-sectional view of the microchannel test section.

classification by making use of the hydraulic diameter, $D_h$. Under this criterion, our channel would be categorised as minichannel since the hydraulic diameter of the channel is located between 200 µm and 3 mm.

To accomplish boiling within the channel whilst enabling visualisation studies, a transparent heating system was required. This was achieved by sputtering a thin tantalum layer onto the exterior wall of the channels. Similar to previous studies [41,49], uniform heating was achieved by coating the four outer surfaces of the high aspect ratio microchannel. The thin tantalum coating provides electrical resistance to produce heating when electricity is supplied whilst maintaining transparency on the visual spectrum. As a result, the flow behaviour could be observed by a high-speed video camera. The channels utilised during the study had a resistance of 2 kΩ. The uniform heating applied in the present work implies that there is no temperature gradient that may induce preferential nucleation and bubble formation. In order to have a better control of the bubble nucleation other techniques such as local resistance variation, surface modification and/or local laser heating are suggested for future works.

A 240 V alternating current transformer was used as a power supply for the test section. It was coupled with a rectifier to convert the alternating current (AC) into direct current (DC). Aluminium foil strips were placed on both channel ends, acting as electric terminals. Crocodile clips were used to connect the terminals to the DC rectifier to create a closed electrical circuit. Two multimeters were installed to measure the voltage and current, respectively. A Kethley 175 Autoranging digital multimeter was connected to measure the current in mA with an accuracy of 0.2%. In addition, a Kethley 192 multimeter was connected in parallel with the circuit to measure the applied voltage accurately with an accuracy of 0.01%. The voltage and current values were recorded to calculate the applied heat flux following Joule's first law.

The microchannel flow boiling bubble behaviour was then captured with a NanoSense MKII high-speed video camera (USA) fitted with a 2.5 mm lens. The camera resolution and frame rate could be adjusted based on the visualisation requirements. To capture the bubble dynamics with the effect of channel confinement in a high aspect ratio channel, the camera was placed above the top surface of the channel normal to the width to length channel plane and hence normal to the flow direction. In both horizontal and vertical upward configurations, the visualisation was always taken from the width to length plane to allow the measurement of the bubble length and width reported in the results and discussion section, which supported the bubble confinement and elongation behaviour analysis. To enhance the contrast during the optical imaging, an LED backlight lighting was installed from the opposite side of the channel. For most recordings, the camera was set on a full resolution of $512 \times 512$ pixels and at a frame rate of 1000 frames per second (fps). The videos consisted of between 8000 and 20,000 images. Although the number of fps adopted may not allow the set up to elucidate the bubble growth during the inertia-driven growth phase for which higher magnification should also be applied, this configuration is actually sufficient to map the profile evolution of the bubble during the different growth regimes for the relatively low heat fluxes investigated. A personal computer, equipped with Dynamic Studio 2015 software, was utilised to operate the camera and monitor the flow visualisation. The software supported various functions such as frame rate and image resolution adjustment, recording settings, and file management.

The inlet and outlet flow conditions were monitored by employing thermocouples and pressure transducers. Two K-type thermocouples were installed to capture the inlet and outlet fluid temperatures. Two pressure transducers were used to record the pressure fluctuation expected during flow boiling. The pressure transducers were coupled with a National Instruments USB-6009 data acquisition unit. The device was connected to a personal computer supported with LabVIEW software. A program was built to convert the voltage values from pressure transducer into accurate pressure readings and record the data during the flow boiling.

The microchannel surface temperature profile was captured with a

Flir 645sc IR camera (Sweden) with thermal sensitivity of 20 mK for a $640 \times 480$ pixels resolution and a maximum frame rate of 25 fps. It was fitted with a Flir TR197909 lens with a focal length of 24.6 mm, allowing the temperature distribution along the entire channel to be imaged and recorded. The current configuration and maximum number of fps are adequate to capture the thermal oscillation caused by bubble elongation process which often occurs in the frequency lower than 3 Hz i.e., period of 0.33 s [38,50,51]. However, higher fps may be needed to capture a more detailed phenomenon for higher fluxes where the bubble dynamics and liquid-vapour interaction become more complex, which are out of the scope of the current work. The emissivity of the IR camera was obtained according to the process described by Madding [52]. During the tests, the average value of the channel emissivity was found to be 0.83. The recorded camera temperature was then compared with the temperature readings obtained from the thermocouples. It was found that the deviation of channel emissivity was 0.02.

### 2.2. Experimental procedure

The experimental procedure was initiated by flushing the flow path and ensuring that the test section was filled with the working degassed fluid as well as so to get rid of all entrapped bubbles. The degassing process was completed by vigorously boiling the working liquid for 1 h. Thereafter, the syringe pump was configured by specifying the syringe size and setting the desired flow rate. The degassed fluid was pumped through the system whilst the voltage was gradually increased until the target value was reached. Once the outlet temperature measurement stabilised at around the fluid saturation temperature (within a minimum variation when compared to the outlet temperature) for 3 min and the desired boiling phenomenon was observed, data recording was initiated. In addition to single bubble growth, the flow pattern for both the inlet and outlet regions was also recorded. The video was then transferred from the camera to the PC, and the sequence of images was extracted. ImageJ software was used to analyse the bubble dynamics seen during the different flow boiling cases. The software was able to convert the raw grayscale images into binary images by choosing a proper threshold value. As a result, several bubble parameters, as shown in Fig. 3, were obtained.

The influence of altering specific operational conditions on the flow boiling behaviour was investigated. This was achieved by accumulating data for a test matrix consisting of different mass flow fluxes, heat fluxes, and two different channel orientations, horizontal and vertical upward flow. The mass fluxes were varied by changing the volumetric flow rate of the pump. Based on the criteria proposed by Lee et al. [53], the flow can be considered a hydrodynamic fully developed flow after 1.22 mm from the inlet for any mass fluxes between 14 and 42 kg m$^{-2}$ s$^{-1}$ equivalent to a Reynolds number between 28.4 and 85.2, respectively. Furthermore, various electrical power was applied to the channel to obtain the different heat flux values. The experimental conditions of the
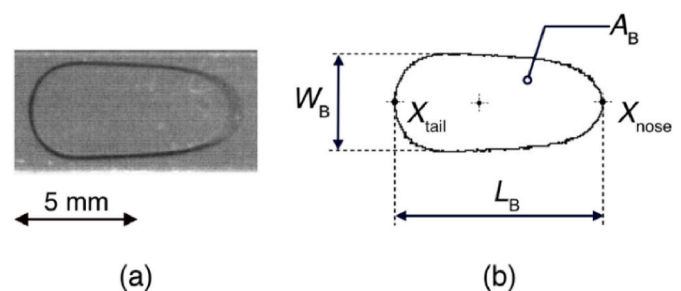


**Fig. 3.** a) Raw image of single bubble b) The liquid-vapour interface after the image processing result and the measured bubble parameters. $A_B$, $W_B$, $L_B$, $X_{tail}$, $X_{nose}$ are, respectively, the area of the bubble, bubble width, bubble length, the bubble nose representing the front position of the bubble, and the bubble tail which is the rear position of the bubble.

present study are shown in Table 2.

It should be noted that in the present study, the channel was uniformly heated and there was no controlled nucleation site in the microchannel. Hence, for the case of single bubble growth analysis, observations were focused on low heat flux cases, between 2.8 kW m$^{-2}$ and 7.0 kW m$^{-2}$ so to minimise the occurrence of numerous nucleation sites. For this investigation, higher heat fluxes are avoided since these would lead to further bubble nucleation and coalescence before the bubble could complete all the reported single bubble growth stages. Since the bubble confinement behaviour is the main interest of this study, only bubbles displaying the elongated bubble phase and departure were considered. To ensure repeatability, three single bubble growth events were observed and analysed for each configuration. Due to the relatively low saturation temperature of the working fluid, no preheating was required to achieve boiling incipience within the channel. The inlet temperature of the liquid was 21.5 °C (±1.5 °C), representing the ambient temperature within the experimental enclosure.

During the experiments, several uncertainties were identified. These uncertainties could mainly be ascribed to the channel dimensions, the technical specification of the measuring devices, and the calibration process. For the parameter that was not directly measured, the uncertainty of the component was determined first. The uncertainties of the bubble parameters were strongly affected by the spatial resolution of the image, depending on the camera setup during the observation. For example, the uncertainty of the bubble diameter measurement was determined by following equation:

$$\frac{\delta D_{B,mm}}{D_{B,mm}} = \sqrt{\left(\frac{\delta D_{B,pix}}{D_{B,pix}}\right)^2 + \left(\frac{\delta CF}{CF}\right)^2} \tag{3}$$

where $D_{B,mm}$ is the bubble diameter measured in mm, $D_{B,pix}$ is the bubble diameter measured in pixel, $CF$ is the calibration factor to convert the measurement in pixel to mm. In terms of heat flux, the uncertainty was obtained as a function of heat transfer efficiency, input power, and the inner channel area. Hence, the uncertainty of those parameters was calculated first before obtaining the uncertainty of the heat flux. The experimental uncertainties are summarised in Table 3.

## 3. Data reduction

The volumetric flow rate, $\dot{V}$, of the syringe pump was converted to a mass flux, $G$, with equation (4):

$$G = \frac{\dot{V}\rho_L}{A_c} \tag{4}$$

where $\rho_L$ is the liquid density, and $A_c$ is the internal cross-sectional area of the channel which is equal to $W_{in} \cdot H_{in}$. Next, the input power, $Q_{input}$, provided by the heating system was calculated based on Joule's first law:

$$Q_{input} = U \cdot I \tag{5}$$

where $U$ is the voltage and $I$ is the current, measured by the respective multimeters. Due to the channel being completely uninsulated, significant heat loss was expected. Thus, the input power differed from the

**Table 2**
Experimental conditions.

| Parameter | Unit | Value |
|---|---|---|
| Hydraulic diameter ($D_h$) | μm | 909 |
| Confinement number ($Co$) | – | 1.05 |
| Bond number ($Bd$) | – | 0.89 |
| Mass flux ($G$) | kg m$^{-2}$ s$^{-1}$ | 14–42 |
| Reynolds number ($Re$) | – | 28.4–85.2 |
| Heat flux ($q$) | kW m$^{-2}$ | 2.8–18.6 |
| Boiling number ($Bo$) | – | $0.78 \times 10^{-3} – 4.61 \times 10^{-3}$ |

**Table 3**
Experimental measurement uncertainties.

| Properties | Unit | Maximum uncertainty |
|---|---|---|
| Pump volumetric flow rate ($\dot{V}$) | ml/hour | 0.5% |
| Thermocouple temperature ($T_{in}, T_{out}$) | °C | ±0.2 °C |
| IR camera measured temperature ($T_w$) | °C | ±2 °C |
| Hydraulic diameter ($D_h$) | mm | 4% |
| Inlet and outlet pressure ($P_{in}, P_{out}$) | mbar | 0.25% |
| Current ($I$) | mA | 0.2% |
| Voltage ($U$) | V | 0.01% |
| Heat Flux ($q$) | W m$^{-2}$ | 6.2% |
| Mass Flux ($G$) | kg m$^{-1}$ s$^{-2}$ | 4.1% |
| Bubble equivalent diameter ($D_B$) | mm | 6.38% |
| Bubble length-to-width aspect ratio ($\beta$) | – | 17.6% |

effective heat absorbed by the liquid. For single-phase flow heating, the effective heat supplied to the liquid, $Q_{eff,sp}$, was determined by equation (6):

$$Q_{eff,sp} = \dot{m}C_p(T_{out} - T_{in}) \tag{6}$$

where $T_{out}$ and $T_{in}$ are the liquid temperature measured at the outlet and inlet sections, respectively, $C_p$ is the liquid-specific heat capacity, and $\dot{m}$ is the mass flow rate equals $\dot{V}\rho_L$.

Under two-phase flow conditions, the heat loss due to convection and radiation was first calculated as done in previous study [54]. Thereafter, the effective two-phase heat flux, $Q_{eff,tp}$, was determined using equation (7):

$$Q_{eff,tp} = Q_{input} - Q_{conv} - Q_{rad} \tag{7}$$

Next, the convective heat loss, $Q_{conv}$, was calculated with equation (8):

$$Q_{conv} = h_{conv}A_{w,out}(T_w - T_{amb}) \tag{8}$$

where $h_{conv}$ is the convective heat transfer coefficient of air at the ambient conditions and it was estimated from the available empirical correlation for natural convection [55,56]. $T_w$ is the average wall temperature measured by the IR camera and $T_{amb}$ is the ambient temperature. The outer surface area, $A_{w,out}$, of the microchannel is calculated with equation (9):

$$A_{w,out} = 2L_h(W_{in} + 2d) + 2L_h(H_{in} + 2d) \tag{9}$$

where $L_h$ is the channel heated length, $W_{in}$ and $H_{in}$ represent the inner width and the height of the channel, respectively, and $d$ is the thickness of the channel.

The radiative heat loss, $Q_{loss,rad}$, were estimated with equation (10):

$$Q_{rad} = \varepsilon\omega A_{w,out}\left(T_w^4 - T_{amb}^4\right) \tag{10}$$

where $\varepsilon$ is the emissivity of the channel and $\omega$ is the Stefan Boltzmann constant.

The heat transfer efficiency, $\varphi$, for each case was calculated by making use of equation (11):

$$\varphi = Q_{eff}/Q_{input} \tag{11}$$

The result of single phase case and two phase case under similar mass flux were compared. A linear trend between effective heat and input power was found in the present study with the value of the $\varphi$ ranging between 0.77 and 0.86. Finally, the effective heat flux, $q$, was calculated using the following equation (12):

$$q = \frac{\varphi Q_{input}}{A_{w,in}} \tag{12}$$

where $A_{w,in}$ is the inner channel surface area.

The flow observation, from the normal direction to the fluid flow, was conducted to obtain visual data on the bubble phenomenon. Next, various bubble parameters were extracted using ImageJ software. To obtain the bubble equivalent diameter, $D_B$, the bubble area, $A_B$, looking from the top as in Fig. 3, was first measured and then equation (13) was used:

$$D_B = \sqrt{\frac{4A_B}{\pi}} \tag{13}$$

Another important parameter was the bubble length-to-width aspect ratio, $\beta$, which was used to characterise the bubble elongation process calculated with the use of equation (14):

$$\beta = \frac{L_B}{W_B} \tag{14}$$

where $L_B$ and $W_B$ are the length and width of the bubble, respectively.

## 4. Result and discussion

### 4.1. Validation

Single phase experiments were carried out in order to check the validation of the system and the methodology adopted in the present work. Two parameters, the pressure drop and the heat transfer coefficient for single-phase were assessed and the results were compared with the available proposed correlations from the literature. Fig. 4 a) shows the result of the calculation of Fanning friction coefficient from the adiabatic experiments and the proposed correlation by Shah and London [56] for rectangular channels and fully developed flow. The Fanning friction factor tends to decrease with the Reynolds number, and a good agreement is found between our experiments and the correlation of Shah and London [56] with a mean absolute error of 16.4%. Next, the single-phase diabatic case was also evaluated to obtain the heat transfer characteristics in the form of Nusselt number versus Reynolds number. Fig. 4 b) shows the Nusselt number obtained from the experiments and its comparison with the correlation proposed by Lee and Garimella [57] with a mean absolute error of 6.5%. The single-phase test results demonstrate that the experimental facility and methodology adopted in the present work can provide accurate results for the flow boiling experiments.

### 4.2. Single bubble dynamics

The dynamics of single bubble nucleation and growth are analysed to understand better the phase-change process and how confinement influences bubble behaviour. Fig. 5 shows the evolution of the bubble diameter for the flow boiling case of $G = 28$ kg m$^{-2}$ s$^{-1}$ and $q = 3.1$ kW m$^{-2}$ under horizontal flow configuration. The upper part of the figure shows the bubble equivalent diameter and its growth rate, whilst the bottom part of the figure depicts the bubble length and width evolution together with the length-to-width aspect ratio.

After bubble nucleation occurs, the small bubble undergoes free growth inside the channel without any restriction. Previous researchers [41,49] discussed the three stages of bubble growth behaviour inside the channel and the first stage refers to the free bubble growth (stage I). In this stage, the bubble growth rate tends to be slow due to the small bubble wall contact area, with a bubble aspect ratio of around 1. It should be noted that most data shown in this stage represents the thermally controlled bubble growth occurring after the rapid occurrence of the inertia controlled bubble growth which ensues in a timescale of less than 1 ms as observed by Bogojevic et al. [38]. The bubble keeps growing until it becomes confined by the channel depth. The second stage is called partially confined bubble growth (stage II), which takes place at $t = 72$ ms. The start of the partial confinement regime is found when the bubble equivalent diameter is 0.5 mm (equal to the channel depth) and as such, the bubble starts experiencing heating from both upper and lower walls. As the bubble-wall contact area increases, the bubble receives more heat leading to a higher evaporation rate, which causes the bubble diameter to increase steadily. The bubble growth rate during this period is higher than that seen during the early stage and keeps increasing. With close inspection of the lower part of Fig. 5, it becomes clear that between $t = 72$ and $t = 200$ ms, the bubble length and width increase similarly with a bubble aspect ratio of 1.

After that, the bubble starts to experience further confinement due to the channel width, although it has not reached the maximum inner channel width of 5 mm, but rather measured approximately 3.2 mm. This confinement causes the evolution of the bubble shape, resulting in the formation of an elongated bubble. In stage III, called the bubble elongation stage, the bubble evolves into an elongated bubble and fills the channel. The transition from stage II to III takes place when the elongation process of the bubble becomes dominant, and the bubble length-to-width ratio equals 1.1, reaching the transition point called the onset of bubble elongation (OBE). After $t = 234$ ms, it is observed that the bubble length grows exponentially while the bubble width growth is
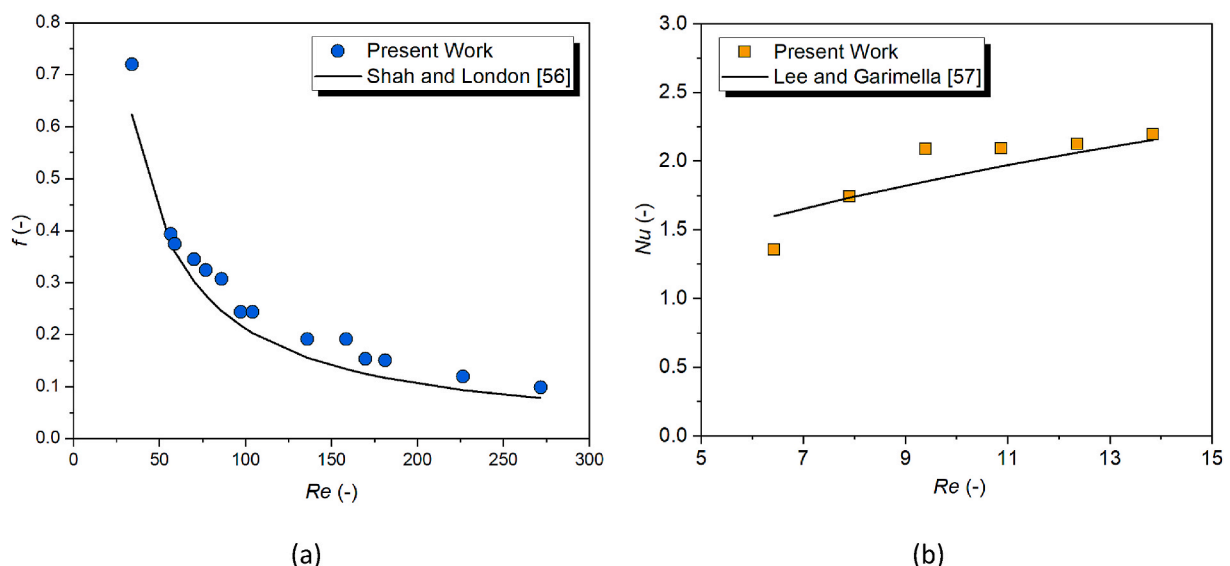


(a)

(b)

**Fig. 4.** The results of single phase experiment a) fanning friction factor versus Reynolds number b) Nusselt number versus Reynolds number.
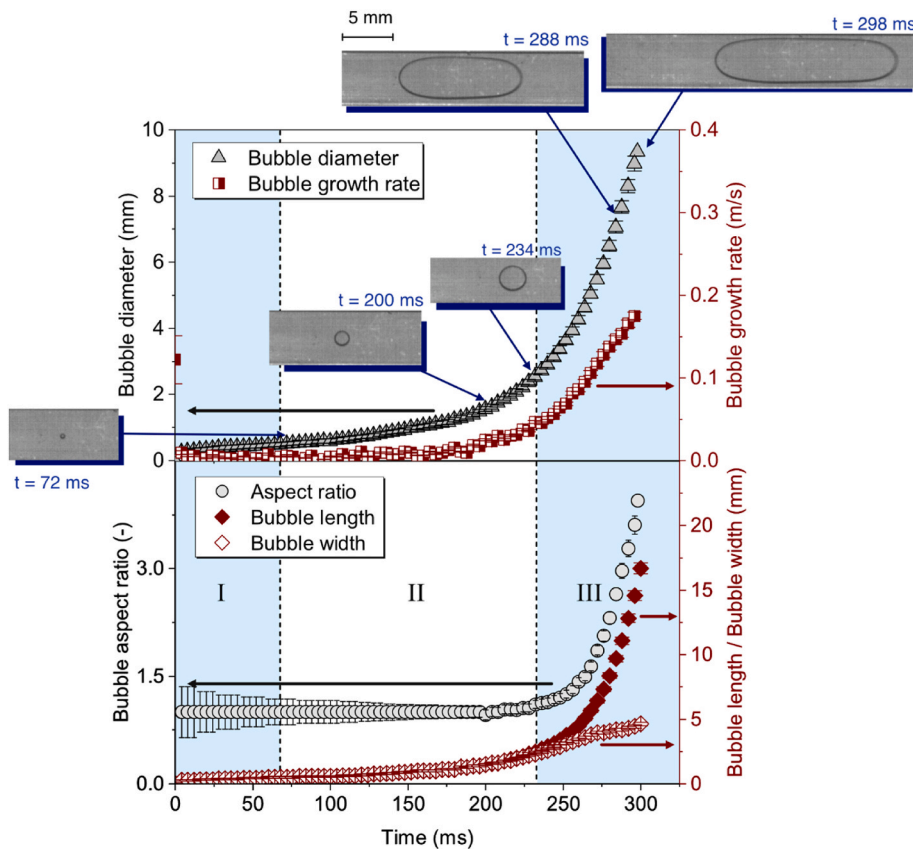
**Fig. 5.** Single bubble profile evolution ($G = 28$ kg m$^{-2}$ s$^{-1}$, equivalent to $Re = 56.8$, $q = 3.1$ kW m$^{-2}$, horizontal flow). The upper part of the figure shows the bubble diameter (up triangle, in mm) and bubble growth rate (half-filled square, in mm/ms). The bottom part of the figure illustrates the bubble length-to-width aspect ratio (circle), bubble length $L_B$ (filled diamond, in mm) and bubble width $W_B$ (empty diamond, in mm). Three bubble growth stages are introduced: free bubble growth (stage I), partially confined bubble growth (stage II), and bubble elongation stage (stage III). The vertical dashed lines represent the transition between the different stages.

restricted by the channel width.

As mentioned previously, various parameters influence the flow boiling characteristics and the accompanying bubble behaviour. The experimental test matrix included different mass and heat flux combinations together with different channel orientations. The influence of these parameters on the bubble dynamics was analysed. Fig. 6 shows the effect of heat flux on the bubble diameter evolution, and it reveals that the bubble growth rate increases with an increase in heat flux, as expected. For a heat flux of 3.1 kW m$^{-2}$, the bubble diameter reaches a size of 4 mm at $t = 270$ ms. However, for a higher heat flux of 7 kW m$^{-2}$, it takes around 80 ms for the bubble to evolve to a similar size. Wang et al. [49] introduced two critical transition times between the bubble growth stages, and this concept is also adopted for this study. Two straight vertical dashed lines, representing the transition points for each case, are shown in Fig. 6. As expected, the critical times for the transitions at high heat flux occur earlier than those at lower heat flux.

After bubble nucleation, the bubble continues receiving energy supplied by the heated wall, causing it to grow in size. The higher heat flux provides more energy to be transferred to the bubble, enhancing the evaporation process. This rapid evaporation at higher heat fluxes continues as the bubble enters the later stages of bubble growth. The bubble experiences both partial and full confinement conditions, and the inner channel walls influence the increased bubble growth rate. As the bubble enters the bubble elongation stage, the bubble surface area will rapidly increase. This phenomenon enhances the heat transfer performance by providing a larger area where the evaporation of thin liquid film between the bubble and wall occurs. However, at the same time, it also has the potential to trigger the occurrence of dry out. Mukherjee et al. [31] explained that dry-out conditions resulted in the early approach of the critical heat flux, whereafter the heat transfer performance deteriorates.

Mass flux is another parameter affecting the bubble evolution and growth, which is represented in Fig. 7. Here, three cases of mass fluxes are compared for the same heat flux of 3.7 kW m$^{-2}$ under a horizontal

flow configuration. The bubble growth, particularly before the elongation process, i.e., while $L_B = W_B$, decreases with an increased mass flux. Furthermore, for increased mass fluxes, the onset of the elongation process is delayed. For example, for a mass flux of 28 kg m$^{-2}$ s$^{-1}$, the bubble takes 100 ms to enter the bubble elongation stage. When the mass flux is increased to 42 kg m$^{-2}$ s$^{-1}$, the bubble only reaches the elongation stage at 350 ms. The relation between bubble growth and mass flux found in this study agreed with previous studies conducted by Yin et al. [58] and Edel and Mukherjee [59]. As the mass flux increases, the liquid can remove more heat from the wall allowing less heat to be transferred to the bubble. In addition, the increased liquid velocity provides an enlarged inertia force around the bubble that acts as a resistance force during the bubble growth process.

Next, we look into the bubble evolution seen during flow boiling at different flow orientations for horizontal and vertical upward flows in Fig. 8. In the case of horizontal flow, represented in Fig. 8 a), initially, the bubble grows uniformly in parallel and perpendicular to the flow directions resulting in a bubble length-to-width aspect ratio equal to 1. During this stage, the nose and tail of the bubble are of a similar shape. It is observed that at $t = 38$ ms, the bubble diameter reaches 0.5 mm. Thereafter, the bubble enters the transition stage from stage I to stage II and starts experiencing partial confinement due to the channel height restricting further uniform growth. At $t = 100$ ms, the bubble maintains $L_B / W_B = 1$ and the diameter increases to 1.96 mm. When the bubble reaches an equivalent diameter of 2.47 mm at $t = 108$ ms, it is observed that the bubble length-to-width aspect ratio slightly increases to 1.1. At this stage, the bubble width is 2.34 mm and the bubble length measures 2.59 mm. The restrictive channel width combined with the liquid flow around the bubble causes further bubble confinement resulting in the onset of the bubble elongation as the transition from stage II to stage III. During stage III, the bubble growth in the direction parallel to the flow direction becomes dominant, and the bubble shapes into an elongated bubble. Similarly, the bubble length-to-width aspect ratio keeps
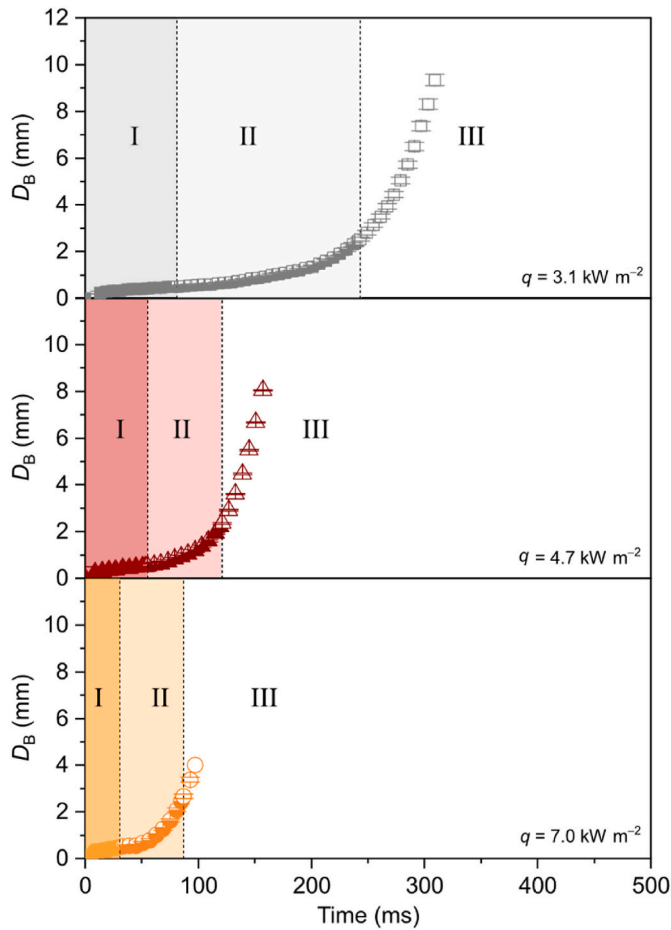
**Fig. 6.** The evolution of the bubble equivalent diameter, $D_B$ (mm), versus time, $t$ (ms), at various heat fluxes for $G = 28$ kg m$^{-2}$ s$^{-1}$, equivalent to $Re = 56.8$, and horizontal flow configuration. Full symbols represent free bubble growth (stage I), the half-bottom-full symbols show the partially confined bubble growth (stage II), and the empty symbols are the bubble elongation stage (stage III). Two vertical dashed lines shown in the Figure illustrate the critical time as a transition point of the bubble growth stage.

**Fig. 7.** The evolution of bubble equivalent diameter at different mass fluxes for $q = 3.1$ kW m$^{-2}$ and horizontal flow configuration. The full symbol represents the free bubble growth. Full symbols depict free bubble growth (stage I), the half-bottom-full symbols represent partially confined bubble growth (stage II), and the empty symbols show the bubble elongation stage (stage III). Two vertical dashed lines shown in the Figure illustrate the critical time as a transition point of the bubble growth stage.

increasing until it reaches a value of 2.34 with an equivalent diameter of 6.14 mm at $t = 136$ ms.

An example of the typical bubble evolution seen for a vertical upward flow case is shown in Fig. 8 b). At $t = 34$ ms, the bubble diameter is approximately 0.5 mm, and the length-to-width aspect ratio equals 1. Initially, the bubble size is small, and the dominant influence of surface tension over the external forces keeps the bubble shape for the vertical and horizontal shapes similar. However, as the bubble grows, a slightly different phenomenon is observed. At $t = 88$ ms, the bubble diameter is around 1 mm, and the bubble length-to-width aspect ratio drops to around 0.9, i.e., slightly elongated perpendicular to the gravity direction. In this case, the bubble volume as well as the buoyancy force increase. In the vertical upward flow, this force directly influences the bubble shape as the flow direction is parallel to the buoyancy forces direction. The bubble experiences slight deformation to form a disk shape in which the bubble length is smaller than the bubble width, i.e., bubble length-to-width aspect ratio <1.0. On the other hand, due to the minimal influence of the buoyancy force, the bubble in the horizontal flow still experiences uniform growth in the length and width direction and maintains its bubble length-to-width aspect ratio of 1.0. Finally, the bubble growth in the width area will be limited by the channel width. Hence the bubble growth in the direction parallel to the flow will be dominant. The bubble enters the onset of bubble elongation (OBE), and the bubble length-to-width aspect ratio increases gradually.

Fig. 9 shows the bubble length-to-width aspect ratio $L_B/W_B$ versus the bubble equivalent diameter $D_B$ for various mass and heat fluxes and the horizontal and vertical upward flow configurations. On one hand, it is apparent that for horizontal flow boiling, the bubble length-to-width aspect ratio tends to be constant before entering the elongation stage once the bubble equivalent diameter is greater than 2 mm. On the other hand, the bubble in the vertical case experiences a slight decrease in bubble length-to-width aspect ratio before evolving into an elongated bubble. For the observed cases, this behaviour starts to occur when the bubble equivalent diameter in vertical flow reaches 0.60 - 1.00 mm, i.e., the smallest of the channel geometries. It is also observed that the onset of bubble elongation (OBE) occurs at a smaller bubble equivalent diameter for the horizontal case in comparison to that seen for the vertical case. For the case $G = 28$ kg m$^{-2}$ s$^{-1}$ and $q = 2.8$ kW m$^{-2}$, the onset of bubble elongation occurs when the bubble diameter is 2.63 mm, whilst in the case of vertical upward flow, the bubble diameter reaches 3.5 mm during the onset of bubble elongation. In addition, Fig. 9 also implies that this trend, including the drop in aspect ratio and the difference between the onset of bubble elongation point, is less pronounced for the lower heat flux for each mass flux. It is because in the higher heat flux, the bubble experiences a shorter period of stage II in which this phenomenon will take place.

After the bubble passes the onset of elongation point, the bubble starts to enter stage III of bubble growth, where the elongated bubble is
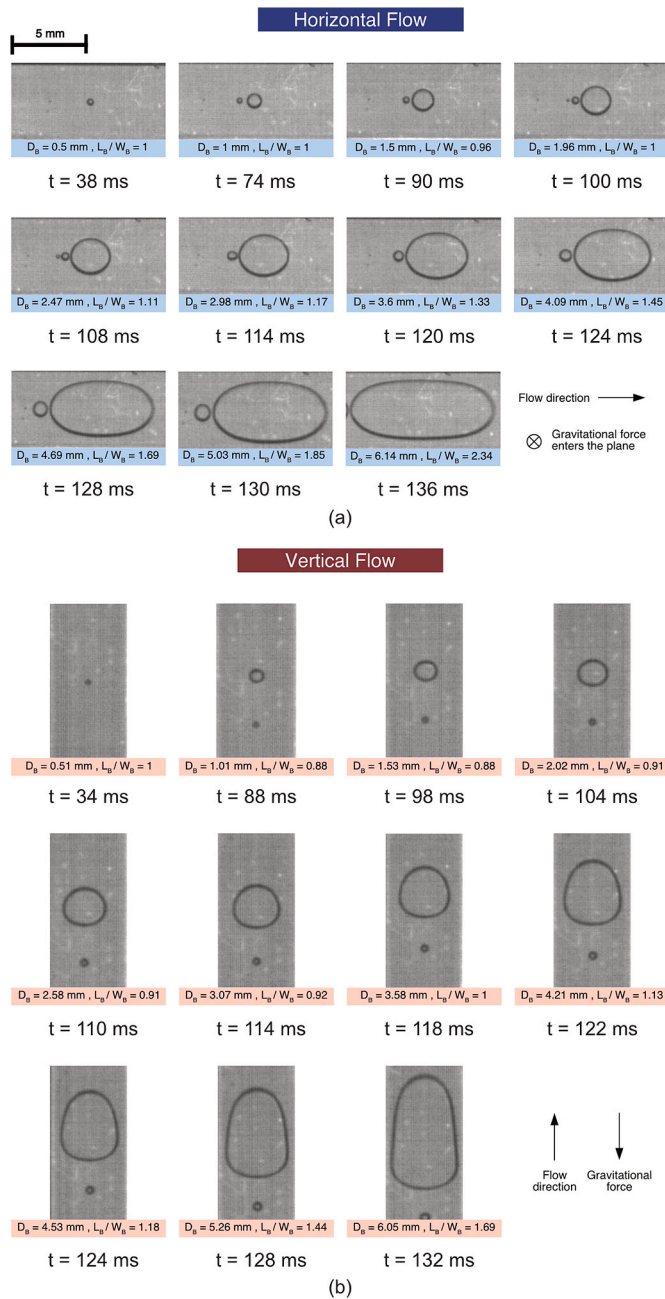
**Fig. 8.** The visualisation of bubble growth for a) horizontal and b) vertical upward flow orientations. ($G = 28$ kg m$^{-2}$ s$^{-1}$, equivalent to $Re = 56.8$, and $q = 2.8$ kW m$^{-2}$). For the horizontal case, the phenomenon was recorded between $t = 38$ ms and $t = 136$ ms. For the vertical upward case, the phenomenon was recorded between $t = 34$ ms and $t = 132$ ms. Each bubble condition is supported by geometry characteristics: bubble diameter ($D_B$) and bubble length-to-width aspect ratio ($L_B/W_B$).

formed. On the left of Fig. 10, an example of the typical shapes of an elongated bubble at $G = 42$ kg m$^{-2}$ s$^{-1}$ and $q = 4.7$ kW m$^{-2}$ for horizontal and vertical upward flow is shown. It is worth noting that for such conditions, the onset of boiling elongation differs quite considerably on the bubble equivalent diameter when comparing horizontal and vertical upward flows, which allows for a more direct comparison. The length of the bubbles is similar and measured approximately as 10 mm. In the horizontal flow case, the bubble nose and tail are similar in shape, whilst an asymmetrical bubble is observed in the vertical flow case. The typical shape of a single bubble at various mass and heat flux combinations is analysed for each of the configurations. To obtain the general shape

trend, the observation was focused on the liquid-vapour interface around the bubble nose and tail. The contours for the different cases and channel configurations are shown in Fig. 10 b. For the bubble nose, although in some cases the bubble nose contour for vertical upward flow is sharper, there is no significant difference between the horizontal and vertical flow cases, whereas significant differences are observed when looking at the shapes of the tail contour. The bubble tail for horizontal flow is similar to the bubble nose, creating an approximately symmetrical elongated bubble, whilst the drag force, buoyancy and fluid movement behind the bubble tail in vertical flow cases cause the bubble tail to form a flat-shaped pattern. The different shapes of the bubble nose and tail observed in the present work also demonstrate the different forces acting at the bubble, such as buoyancy and flow inertia, which may result in the apparent difference between the front and rear contact angles, i.e., upstream region and downstream region, as suggested by Sinha et al. [60,61].

The effect of channel orientation on the bubble nose velocity is also analysed. Fig. 11 illustrates the results plotted for the two configurations considered and two heat and mass flux combinations. In general, the bubble nose velocity increases along with the increase in the bubble diameter. When the bubble equivalent diameter is smaller than 2 mm, the bubble nose moves with a similar velocity along the channel for both configurations. However, as the bubble increases in size, the bubble for vertical upward flow configuration moves faster in comparison to that observed during horizontal flow configuration. Wang et al. [62] discussed how buoyancy influenced the bubble movement and suggested that the enhancement effect that occurred for upward flow orientations was due to flow inertia being concurrent with the buoyancy force. Nicklin [63] proposed a bubble movement model that supported that statement and suggested that the bubble movement and velocity within a channel were influenced by liquid movement and buoyancy. In the right axis of Fig. 11, the relation between buoyancy force and bubble diameter is shown. The buoyancy force is calculated by equation (15).

$$F_b = (\rho_L - \rho_G)V_B g \tag{15}$$

where $\rho_L$ and $\rho_G$ are the density of the liquid and vapour phase, $V_B$ is the volume of the bubble, and $g$ is the gravitational acceleration. As heat flux is applied, a small bubble nucleates within the channel. As it receives more heat, the evaporation process causes the bubble volume to increase, and the buoyancy effect begins to play a more significant role in the forces acting on bubble and governing its movement and velocity. Representation of the bubble nose velocities and buoyancy forces in Fig. 11 illustrate quite well how the buoyancy force results in accelerated upward bubble movement for vertical upward flow cases, whilst no significant gravity effects are seen for the horizontal flow cases.

### 4.3. Flow patterns

Both Figs. 12 and 13 depict snapshots of the flow boiling visualisation at various heat and mass flux combinations for the case of vertical upward flow. Fig. 12 focuses on the channel inlet section from $z = 0$ mm up to $z = 20$ mm, whilst Fig. 13 pictures the channel outlet section from $z = 33$ mm up to $z = 53$ mm. The visualisation results were analysed to determine the flow patterns under particular conditions. Thereafter, the flow patterns found during the study were compared to some available flow pattern maps proposed by previous studies.

In the inlet area, slug flow is observed in most cases. Slug flow is characterised by the presence of a liquid-dominant phase, called the liquid slug, and the vapour-dominant phase in the form of an elongated bubble. For low heat fluxes, for example, in the case of $G = 14$ kg m$^{-2}$ s$^{-1}$ and $q = 2.8$ kW m$^{-2}$, the tail of an elongated bubble is observed at the channel inlet section. Bubble nucleation normally occurs in the middle or outlet section of the channel. The bubble grows in both the downstream and upstream directions, triggering flow reversal. As the heat flux is increased, the liquid receives more energy, resulting in the
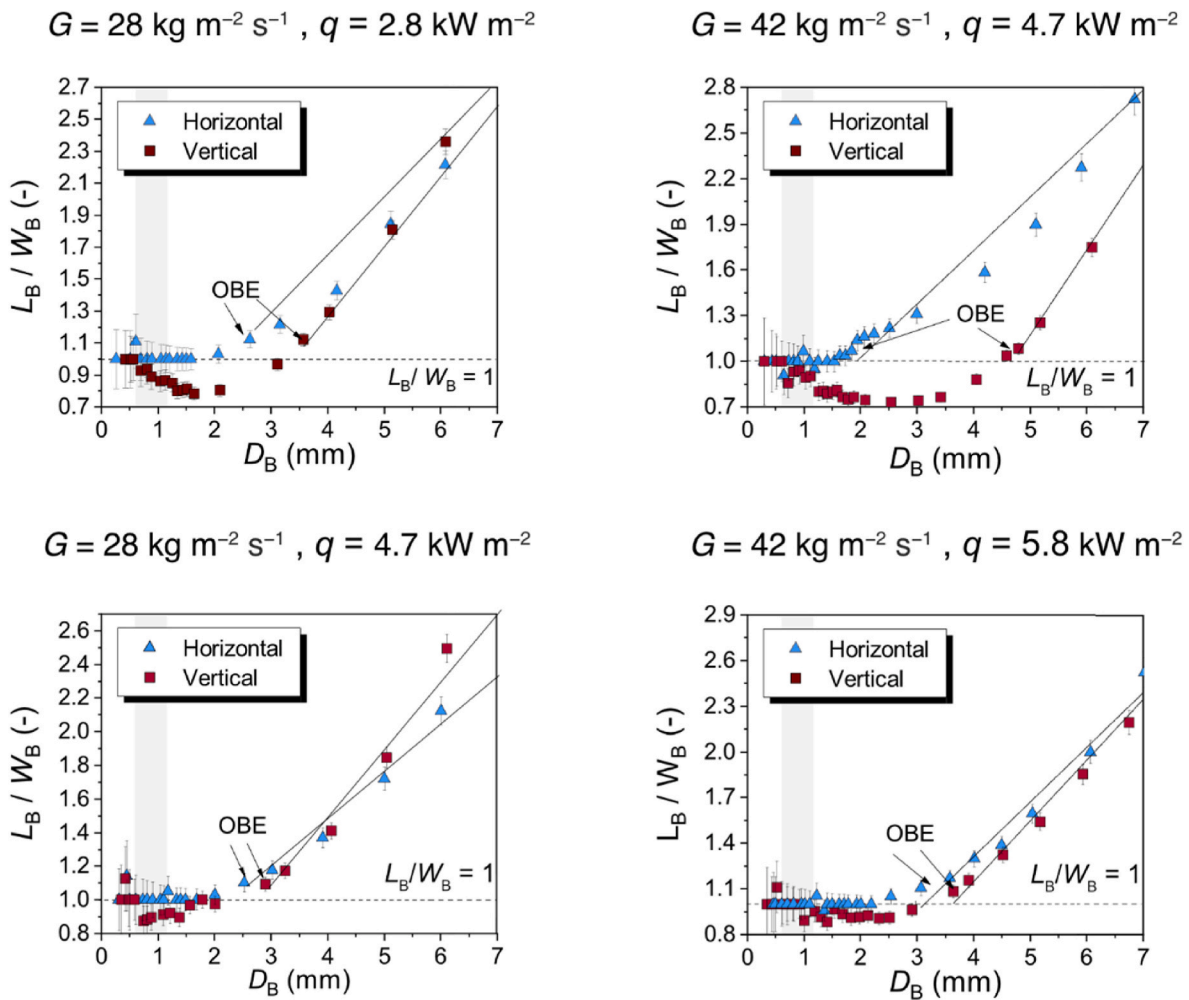
**Fig. 9.** Bubble length-to-width aspect ratio, $L_B/W_B$, for (blue triangles) horizontal and (red squares) vertical upward flow configurations versus bubble equivalent diameter, $D_B$ (mm), for $G = 28$ and $48$ kg m$^{-2}$ s$^{-1}$, equivalent to $Re = 56.8$ and $85.2$, and different heat fluxes, $q$ (kW m$^{-2}$), OBE represents the onset of boiling elongation, solid line is the linear relation $L_B/W_B$ to $D_B$, and dotted horizontal line is the $L_B/W_B = 1$.

nucleation site shifting forward to the middle and the end of the inlet section. Further increase in the heat flux, as shown in the case of $G = 14$ kg m$^{-2}$ s$^{-1}$ and $q = 9.2$ kW m$^{-2}$, results in the nucleation site being close to the channel inlet ($z = 0$ mm). This phenomenon was also observed by previous researchers [11,64]. In addition, the liquid-vapour interface at high heat flux tends to be more wavy compared to that observed at low heat fluxes. In the outlet section, as shown in Fig. 13, three different flow patterns are observed in the channel outlet section: slug flow, churn flow, and annular flow. Slug flow is found at low heat fluxes. As the heat flux increases, the bubble grows faster and more bubble nucleation sites are activated. The stability of the liquid-dominant phase is disrupted, and the liquid-vapour mixing zone is formed. These characteristics correlate to churn flow, which acts as the transition from intermittent flow to annular flow. Further increases in the heat flux heighten the vapour quality in the channel, leading to the observation of annular flow.

The dominant flow patterns observed in the outlet section for both channel configurations are plotted in Fig. 14, with the mass flux and heat flux as the horizontal and vertical axes, respectively. The graph reveals that the combination of mass flux and heat flux in this experimental study produces three flow patterns: slug, churn, and annular flow. No bubbly flow is observed in this study due to the sudden bubble growth as soon as nucleation occurs. After the bubble experiences full confinement, the rapid bubble elongation process occurs, followed by the rewetting process before the next nucleation event takes place. Hence,

the tiny bubble, which is strongly associated with bubbly flow, is only observed in the early stage of bubble growth. This phenomenon was also seen by previous researchers such as Edel and Mukherjee [59] and Markal et al. [65]. The mass flux also plays an important role in the absence of bubbly flow. Higher mass flux allows the bubble to flow to the outlet section before experiencing partial and full confinement. A study conducted by Harichian and Garimella [43] also suggested that bubble confinement was observed in channels at low mass flux but not at high mass flux. These researchers suggested that the transition from confined slug flow to unconfined bubble flow was influenced by the Reynolds number.

As the mass flux is increased from 14 to 42 kg m$^{-2}$ s$^{-1}$, it is found that the transition between slug flow and churn flow, and between churn flow and annular flow, occurs at higher heat fluxes. For instance, in the case with $G = 14$ kg m$^{-2}$ s$^{-1}$, the transition from slug flow to churn flow takes place between $q = 2.7$ kWm$^{-2}$ and $q = 3.6$ kW m$^{-2}$, whilst for $G = 28$ kg m$^{-2}$ s$^{-1}$, this transition occurs only after a heat flux of 7.0 kWm$^{-2}$. This phenomenon is ascribed to the ability of higher mass fluxes to carry more heat. Higher heat fluxes are needed to activate more nucleation sites and heighten the vapour quality inside the channel so that churn flow becomes dominant.

By comparing the two graphs presented in Fig. 14, the effect of channel orientation on flow pattern development is investigated. The trends discussed already are found to be similar for both the horizontal and vertical upward flow configurations. This similar trend is found to
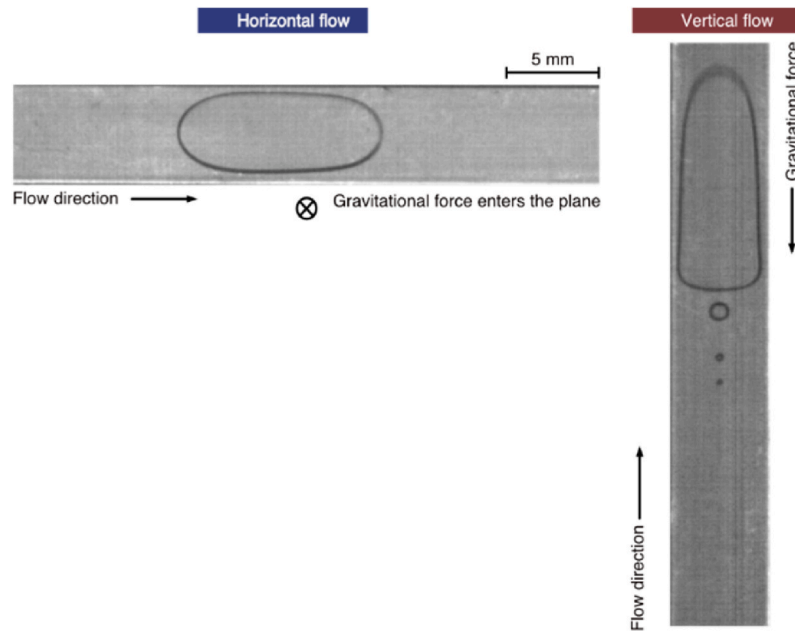
(a)
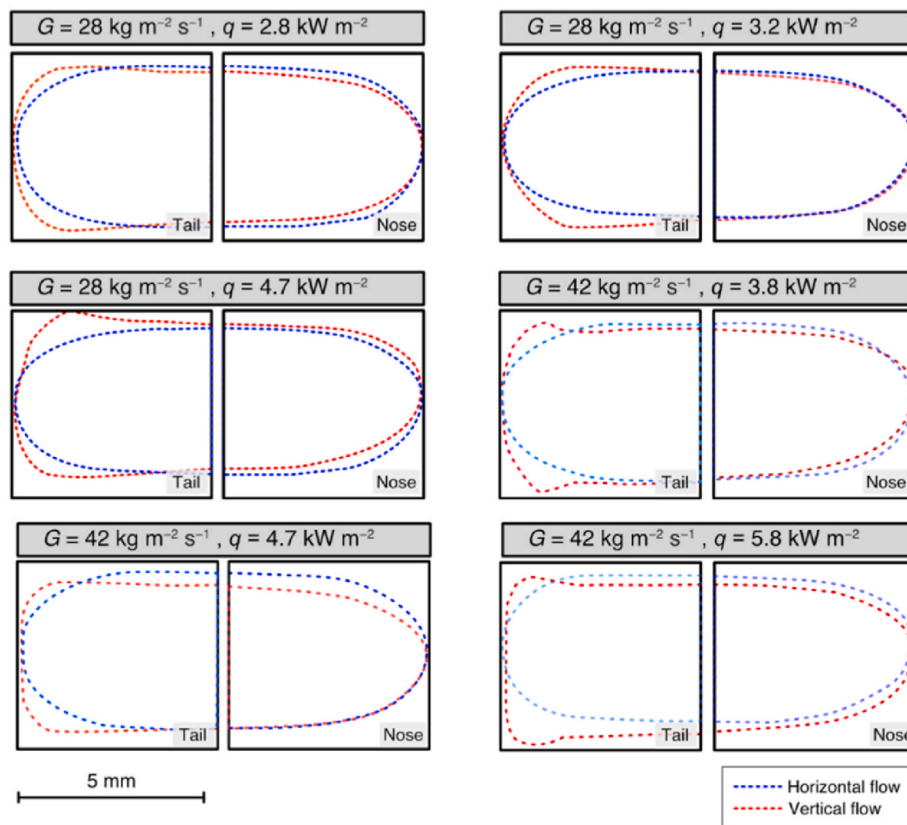


(b)

**Fig. 10.** a) Typical bubble shape in horizontal and vertical flow ($G = 42$ kg m$^{-2}$s$^{-1}$, equivalent to $Re = 85.2$ and $q = 4.7$ kW m$^{-2}$) b) The liquid-vapour interface in the bubble nose and bubble tail regions. The blue dashed line represents for the horizontal flow case, and the red dashed line is the liquid-vapour interface for the vertical flow case ($G = 28$ and $48$ kg m$^{-2}$ s$^{-1}$, equivalent to $Re = 56.8$ and $85.2$, $q = 2.8$–$5.8$ kW m$^{-2}$).
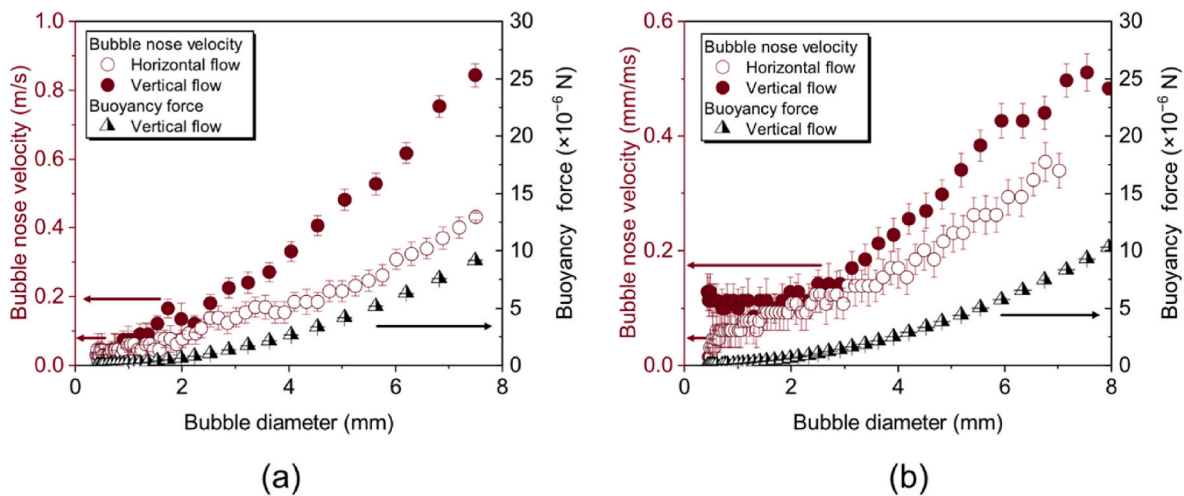
**Fig. 11.** Comparison of bubble nose velocity (left axis, in mm/ms) and buoyancy force (right axis, in N) versus bubble equivalent diameter, $D_B$ (mm), in horizontal and vertical flow configurations for (left) $G = 28$ kg m$^{-2}$ s$^{-1}$, equivalent to $Re = 56.8$, and $q = 2.8$ kW m$^{-2}$, and (right) $G = 42$ kg m$^{-2}$ s$^{-1}$, equivalent to $Re = 85.2$, and $q = 4.7$ kW m$^{-2}$.
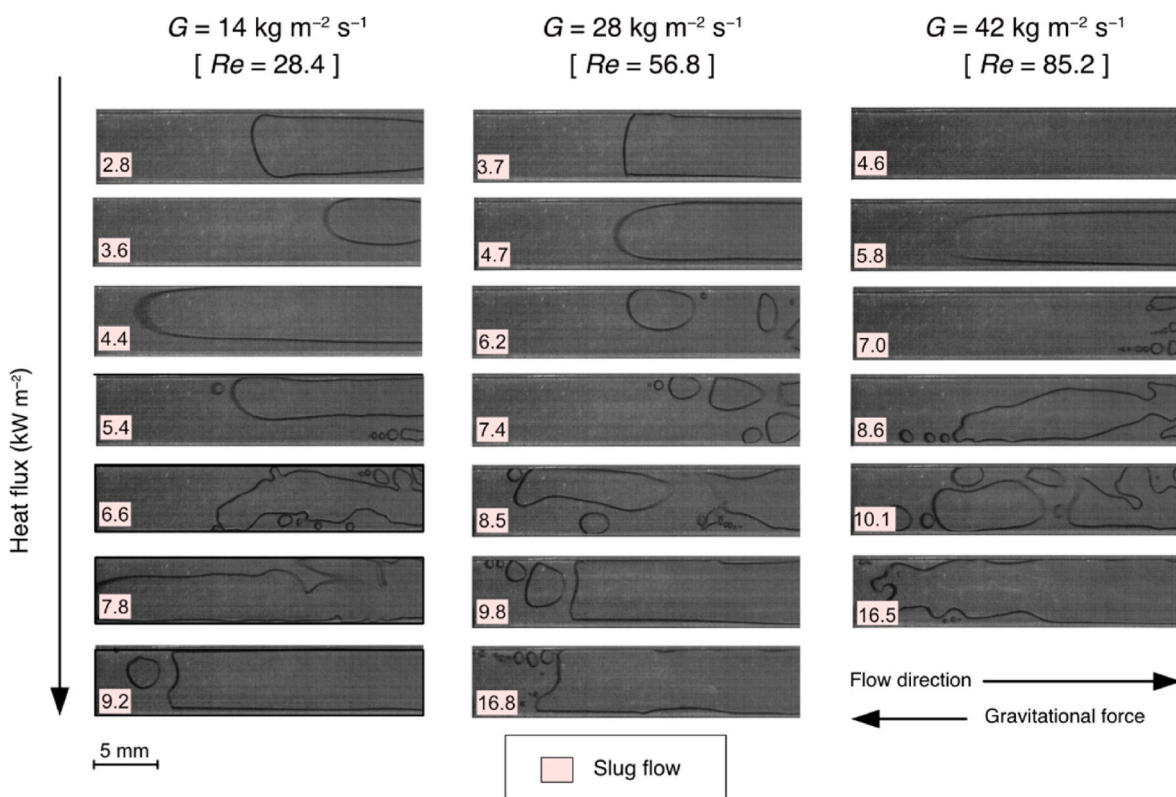


**Fig. 12.** Flow visualisation of channel inlet section ($z = 0$ mm up to $z = 20$ mm) at different mass fluxes, $G$ (kg m$^{-2}$ s$^{-1}$), or Reynolds number, and heat fluxes, $q$ (kW m$^{-2}$), under steady-state condition for vertical upward flow. The number inside the box represents the value of heat flux.

be true due to the single bubble behaviour not being the only factor influencing the flow pattern transitions. The bubble nucleation that occurs along the channel, as well as the coalescence process, also plays an important role in the stability of the liquid slug phase that can trigger the transition from slug to churn and churn flow to annular flow. Costa-Patry and Thome [32] and Costa-Patry et al. [66] suggested that the slug to annular flow pattern transition was affected by various factors, including the heat flux as well as the latent heat of the fluid. This finding highlighted the importance of bubble nucleation, bubble coalescence and the evaporation process during flow pattern development.

### 4.4. Flow map regimes literature comparison

Due to bubble behaviour having such a significant impact on thermal performance and system pressure drop, numerous efforts have been made to predict the flow patterns seen during microchannel flow boiling based on various parameters. In this section, the observed flow pattern will be compared with some selected proposed flow pattern maps from previous investigations which are summarised in Table 4. Due to the similar trend between horizontal flow and vertical flow, as suggested in Fig. 14, the comparison was made by taking the horizontal flow data set
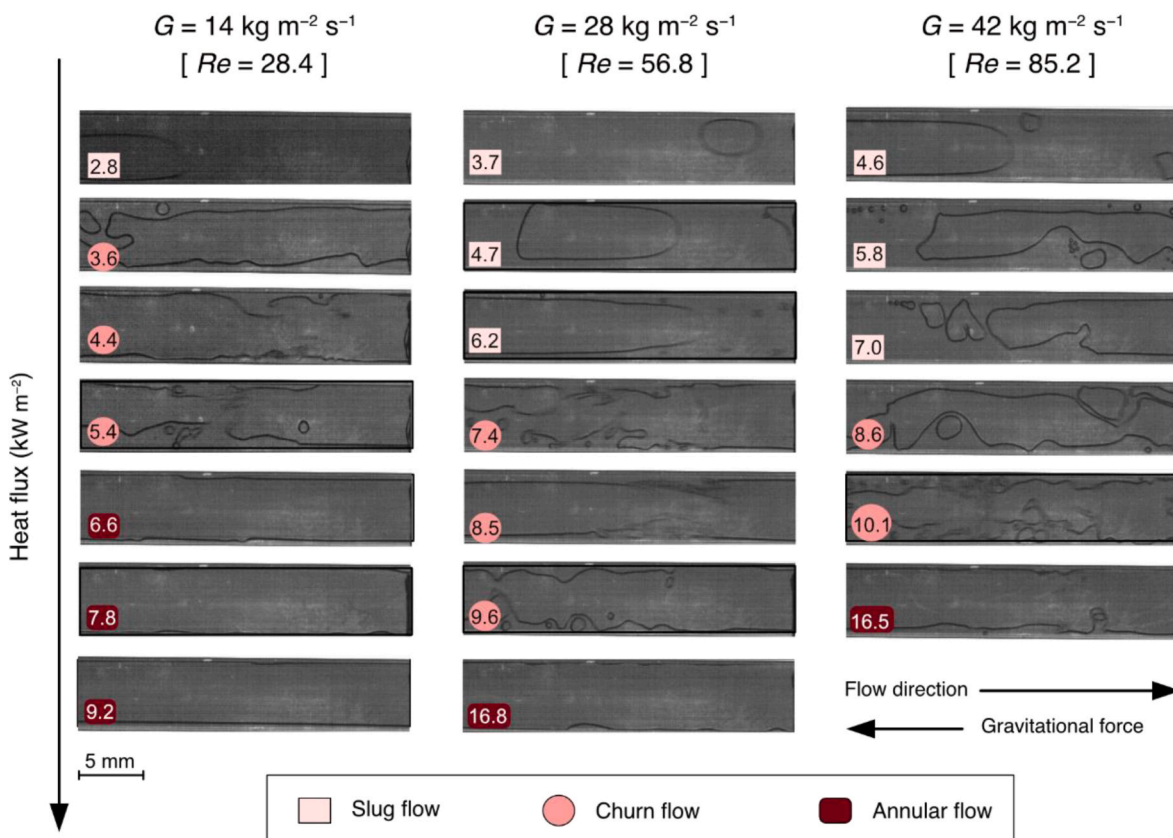
**Fig. 13.** Flow visualisation of channel outlet section for ($z = 33$ mm up to $z = 53$ mm) at different mass fluxes, $G$ (kg m$^{-2}$ s$^{-1}$), or Reynolds number, and heat fluxes, $q$ (kW m$^{-2}$), under steady state condition for vertical flow. The different colour code of the heat flux label illustrates the two-phase regime taking place. The number inside the colour label shows the value of heat flux.



    (a)                                           (b)
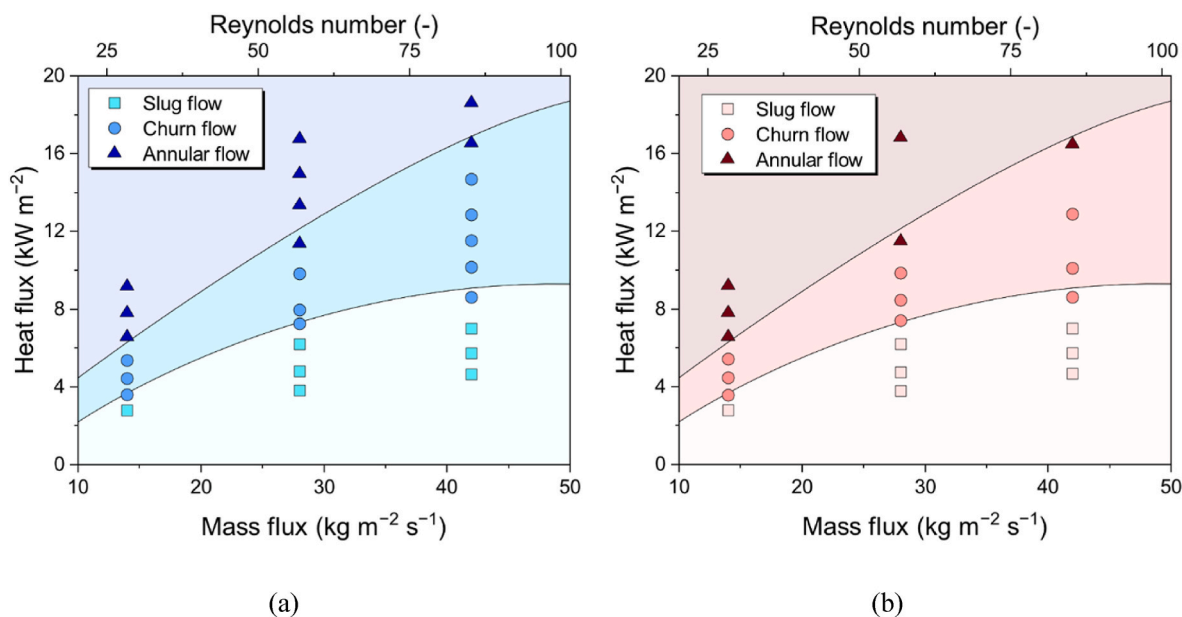
**Fig. 14.** Observed flow patterns (squares) slug flow, (circles) churn flow and (up-triangles) annular flow function of mass flux, $G$ (kg m$^{-2}$ s$^{-1}$), or Reynolds number, and heat flux, $q$ (kW m$^{-2}$), in the outlet section for (left) horizontal flow case and (right) vertical flow case.

to represent the current experimental data.

    One of the characteristics of two-phase flow in microscale channels is the dominance of inertial force and surface tension. Zhao and Rezkallah [67] used the Weber number of the liquid and gas phases, representing the ratio of inertial force to surface tension, to develop a two-phase flow

pattern map in microgravity conditions. The experiment was conducted in microgravity conditions and utilised a single circular channel with an inner diameter of 9.53 mm under a vertical upward flow configuration. The four flow patterns observed in the study were bubble flow, slug flow, frothy annular flow, and annular flow. The flow patterns were classified

**Table 4**
The general information, including the channel condition, geometry, and working fluid, of flow pattern maps that are used as a comparison in the present study.

| Authors | Horizontal and Vertical Axis of Flow pattern map | Fluid | Channel condition and geometry | |
|---|---|---|---|---|
| | | | Channel type | Details of Geometry and additional notes |
| Zhao and Rezkallah [67] | $We_{SL}$ vs $We_{SG}$ | Air-water | - Single channel<br>- Vertical upward flow | - Circular channel: $D_H = 9.53$ mm<br>- Microgravity condition |
| Akbar et al. [42] | $We_{SL}$ vs $We_{SG}$ | Air-water | - Single channel flow<br>- Horizontal and vertical upward flow | - Based on numerous available experimental data<br>- Circular and triangular channels.: $D_H = 0.866$–1.6 mm |
| Revellin and Thome [68] | $X$ vs $G$ | R-134a and R-245fa | - Single channel<br>- Horizontal flow | - Circular channel: $D_H = 0.509$ and 0.709 mm |
| Harirchian and Garimella [43] | $Bd^{0.5} \cdot Re$ vs $Bo \cdot Re$ | FC-77 | - Parallel channels<br>- Horizontal flow | - Rectangular channels, $D_H = 0.96$–7.07 mm<br>- $\alpha = 1.05$–15.55 |
| Zhuang et al. [69] | $X_{tt}$ vs $We^*$ | R-170 | - Single channel<br>- Horizontal flow | - Circular channel $D_H = 4$ mm |

into three regions based on the dominant force, namely the surface tension region (bubble and slug flow), intermediate region (frothy slug to annular flow), and inertia region (annular flow). The transition from the surface tension to intermediate regions occurred at gas/vapor superficial Weber number, $We_{SG}$, of approximately 1. In addition, $We_{SG} \approx$ 20 was chosen to represent the onset of the inertia region.

Fig. 15 a) depicts a comparison between the flow pattern map proposed by Zhao and Rezkallah [67] and the present study's results. Close observation of experimental data and proposed flow pattern transition lines show that for higher mass flux, *i.e.*, high $We_{SL}$, the transition from the surface tension region to the intermediate region shows quite good agreement. Some of the churn flow observed in the present data is located in the intermediate region. However, the flow pattern map overpredicts the transition for low mass flux cases. The proposed flow pattern map suggested that the transition of the flow region is purely affected by the gas superficial velocity in the form of $We_{SG}$. However, the current study proves that the transition lines are influenced by both the liquid and gas superficial velocities. These findings are also observed by Rezkallah [70] when plotting an experimental database to the flow pattern map, producing a linear transition line with an exponential 1:4 positive slope ($We_{SG} \propto We_{SL}^{0.25}$). The applicable transition line for the present work is found to follow a $We_{SG} \propto We_{SL}^{0.55}$ exponential relation for both slug-to-churn and churn-to-annular flow transitions, as indicated in Fig. 15 a).

Akbar et al. [42] collected available experimental data on adiabatic air-water flow to propose a flow pattern map consisting of an inertia-dominated region, a transition region, and a surface

tension-dominated region. The hydraulic diameter for the circular and triangular channels was between 0.867 mm and 1.6 mm. Both vertical and horizontal flow cases were considered in a single flow pattern map which showed that the effect of channel orientation on flow pattern development was negligible. The transition line for the surface tension region is written in eq. (16). In addition, the annular flow zone and dispersed flow zone are expressed by eq. (17) and eq. (18), respectively.

$$We_{SG} \leq 0.11 We_{SL}^{0.315} \; ; \; \text{for } We_{SL} \leq 3.0$$
$$We_{SG} \leq 1; \text{ for } We_{SL} > 3.0 \tag{16}$$

$$We_{SG} \leq 11.0 We_{SL}^{0.14}$$
$$We_{SL} \leq 3.0 \tag{17}$$

$$We_{SL} > 3.0$$
$$We_{SG} > 1.0 \tag{18}$$

Next, Fig. 15 b) shows the comparison between our experimental data and the flow pattern map proposed by Akbar et al. [42]. The proposed flow pattern map inaccurately predicts the current experimental data, where all our data falls within the transition region. The transition line of the annular flow is higher compared to the fitted transition line of the present work. On the other hand, the change of the surface tension-dominated region to the transition region occurs earlier. According to Akbar et al. [42], the large area of the transition region of the flow pattern map consisted of various complex flow patterns that were observed in previous studies. The different approaches to flow pattern definition and the scarcity of data make the detailed characterisation of
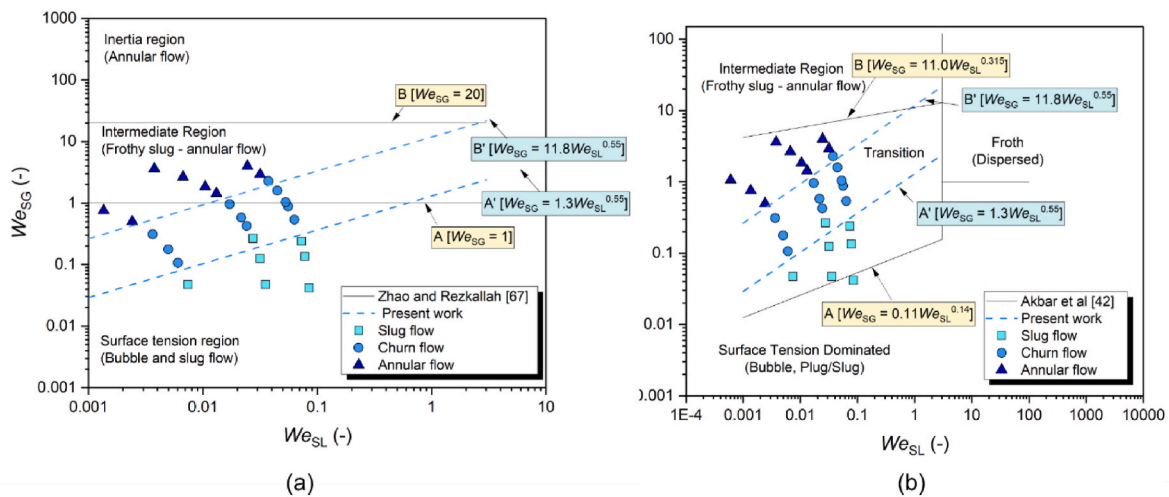


**Fig. 15.** The comparison of experimental data with flow pattern map represented as $We_{SG}$ versus $We_{SL}$ proposed by a) Zhao and Rezkallah [67] and b) Akbar et al. [42] For each figure, the solid lines represent the transition between regimes proposed by the flow pattern map and the dashed lines show the transitions between slug flow, churn flow and annular flow reported in this work.

the flow regimes difficult.

Revellin and Thome [68] introduced a diabatic flow pattern map to identify the flow boiling characteristics using a database that consisted of two types of refrigerant, R-134a and R-245fa, inside a circular tube with a hydraulic diameter of 0.509 and 0.709 mm under horizontal configuration. The observed flow patterns were classified into three flow regimes: the isolated bubble regime (IB), coalescence bubble regime (CB), and annular regime (A). The transition criteria between regimes were described by a combination of non-dimensional numbers such as the Reynolds number, Boiling number, and Weber number, and the representation made use of the mass flux, $G$ (kg m$^{-2}$ s$^{-1}$), versus vapour quality, $X$. On one hand, the transition line between the isolated bubble regime and coalescence bubble regime was calculated as shown in equation (19), whilst the transition line between the coalescence bubble regime and the annular regime was correlated as shown in equation (20). Equation (19) shows that the heat flux, represented by the Boiling number, plays an important role in the transition between the isolated bubble region and the coalescence bubble region. The increase in heat flux enhances the rate of bubble nucleation which enlarges the isolated bubble region. On the other hand, as shown in equation (20), the transition from the coalescing bubble region to the annular flow region is not affected by the heat flux as per the absence of the Boiling number in the equation.

$$X_{\frac{IB}{CB}} = 0.763 \left( \frac{Re_{lo}Bo}{We_{go}} \right)^{0.41} \tag{19}$$

$$X_{\frac{CB}{A}} = 0.00014 \, Re_{lo}^{1.47} We_{lo}^{-1.23} \tag{20}$$

Fig. 16 shows the comparison between the experimental data and the flow pattern map proposed by Revellin and Thome [68]. The transition between the isolated bubble regime and coalescence regime successfully predicts the transition between the slug and churn flow patterns reported in the present study. Slug flow is located in the isolated bubble regime, whilst churn flow is found in the coalescing bubble regime. Slug flow can correctly fall within either the isolated bubble or coalescing bubble regimes, depending on the bubble velocity and coalescence frequency. The isolated bubble regime also consists of bubbly flow that is not observed in the present study. As the vapour quality increases, the flow pattern changes into churn flow and is classified as being part of the coalescing bubble regime, where the bubble coalescence rate is larger than the bubble nucleation rate. In terms of the annular flow regime, the flow pattern map transition line completely overpredicts our experimental data. The range of mass fluxes that were used to construct the flow pattern map was, however, higher than those of the present study, influencing the accuracy of the transition line for lower mass flux cases. Furthermore, Revellin and Thome [68] also pointed out the need for further studies to capture and analyse the instability and flow reversal phenomena which occur at low mass fluxes.
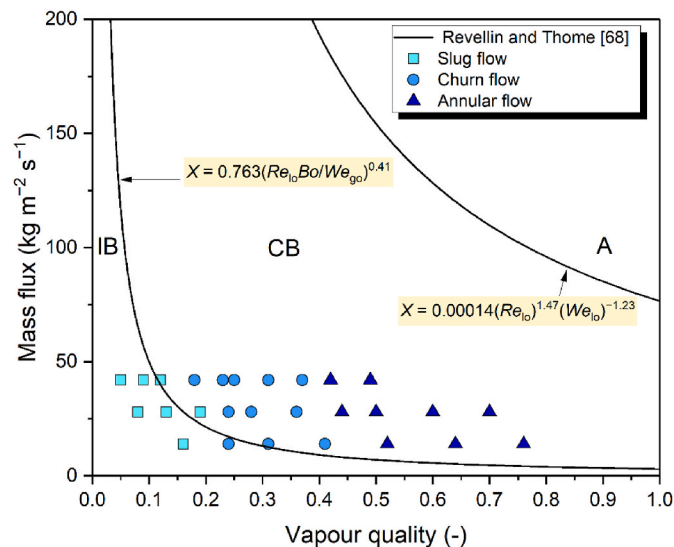
Another diabatic two-phase flow regime map was proposed by Harirchian and Garimella [43,44]. The experimental data of flow boiling of FC-77, covering a wide area of parallel microchannel dimension ($D_h$ = 0.96–7.07 mm), mass flux, and heat flux, was used to propose a flow pattern map which was divided into four regions: confined slug, bubbly, churn/confined annular, and churn/annular/wispy annular. Three dimensionless numbers were used to describe the flow pattern development, namely the Bond number, Boiling number, and Reynolds number. In addition, two transition lines were proposed. The first transition line, described as the convective confinement number, was used to define the transition to confined flow and was affected by the mass flux, channel cross-sectional area, and fluid surface tension. This first transition line was calculated with equation (21):

$$Bd^{0.5} \times Re = 160 \tag{21}$$

The second transition line between bubble or slug flow to alternating churn/annular or churn/whispy annular flow was determined with equation (22):

$$Bo = 0.017 \left( Bd^{0.4} \times Re^{-0.3} \right) \tag{22}$$

Fig. 17 depicts the comparison of the experimental data with the flow pattern map of Harirchian and Garimella [43]. For the current study, no bubbly flow is observed with confined slug and churn/annular flows as the only observed flow patterns. The occurrence of confined slug and churn/annular flow is well predicted by the flow pattern map since all data is located on the left side of the line of convective confinement number $Co = 160$. However, it is seen that the line drawn between slug flow and the churn/annular flow overpredicts the transition values compared to our experimental data. The blue dashed line represents the fitted transition line of the present data, and although the slope of the line is similar, the position is lower compared to the proposed flow pattern map. This may be due to the different experimental conditions of the present study. For example, the present study has a longer heated



**Fig. 16.** The comparison of experimental data with a flow pattern map represented as mass flux, $G$ (kg m$^{-2}$ s$^{-1}$), versus vapour quality, $X$, where solid lines represent the transition between isolated bubble (IB), coalescing bubble (CB) and annular (A) regimes proposed by Revellin and Thome [68].
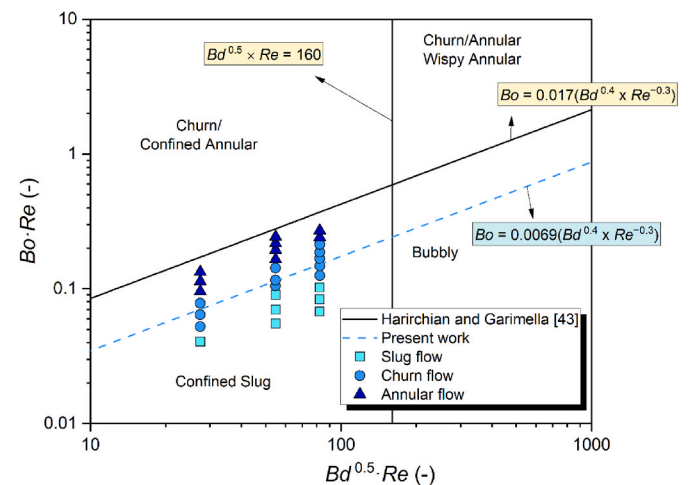


**Fig. 17.** The comparison of experimental data with the flow pattern map, $Bd^{0.5}$ · $Re$ versus $\cdot Re$, proposed by Harirchian and Garimella [43]. The map is divided into four regions: the confined slug, the confined annular/churn, bubbly, and churn/annular. The solid lines depict the transition between the region. The dashed line shows the fitted transition line for the confined slug to the confined annular for the present work.

channel length compared to the experiments conducted by Harirchian and Garimella [43]. At a similar heat flux, the working liquid absorbs more heat causing a higher vapour quality in the outlet. Hence, the transition from the slug flow to the churn flow/annular flow occurs earlier.

Zhuang et al. [69] developed a two-phase flow pattern map that covered various saturation pressures, ranging between 1.5 MPa and 2.5 MPa. R170 was used as the working fluid, and the experiments were conducted within a circular tube with a 4 mm inner diameter. The proposed flow pattern map included important fluid properties such as surface tension. For the vertical axis, a modified Weber number, $We^*$, was used and is defined in equations (23) and (24):

$$We^* = 2.45 \frac{Re_G^{0.64}}{Su_G^{0.3}\left(1 + 1.09X_{tt}^{0.039}\right)^{0.4}} \ ; \ \text{for } Re_L \leq 1250 \tag{23}$$

$$We^* = 0.85 \frac{Re_G^{0.79}X_{tt}^{0.157}}{Su_G^{0.3}\left(1 + 1.09X_{tt}^{0.039}\right)^{0.4}} \ ; \ \text{for } Re_L > 1250 \tag{24}$$

where $X_{tt}$ is defined as the Lockhart–Martinelli parameter turbulent liquid-turbulent vapour flows, and $Su_G$ represents the vapour Suratman number defined in equation (25):

$$Su_G = \frac{\rho_G \sigma D_H}{\mu_G^2} \tag{25}$$

Furthermore, the Lockhart-Martinelli parameter (turbulent liquid – turbulent vapour), $X_{tt}$, was used for the horizontal axis. The flow pattern map was divided into five flow regimes: slug flow, plug flow, transition, wavy annular flow, and smooth annular flow. The transition lines between those flow patterns were described in equations 26–29:

Smooth annular - wavy annular flow

$$We^* = 29.25X_{tt}^{0.27} \tag{26}$$

Wavy annular - transition flow

$$We^* = 18.91X_{tt}^{0.33} \tag{27}$$

Transition - slug flow

$$We^* = 9.62X_{tt}^{0.35} \tag{28}$$

Slug - plug flow

$$We^* = 4.38X_{tt}^{0.45} \tag{29}$$

Fig. 18 shows the comparison of the present experimental data with the flow pattern of Zhuang et al. [69]. The results demonstrate that the proposed flow pattern cannot accurately predict the present experimental data well. In general, the slope of the proposed transition lines seems representative. However, almost all data is located within the annular flow pattern region. To develop the flow pattern map, Zhuang et al. [69] stressed the importance of including the fluid surface tension in the form of modified Weber numbers. The experimental database utilised three different operating conditions, resulting in various surface tension values ranging between 2.99 and 5.61 mN m$^{-1}$ which is lower than the surface tension of the working liquid used in the present study. Soliman [71] explained that surface tension plays an important role in flow pattern transition since it acts as a stabilising force. This may explain the tendency of the lower transition line of Zhuang et al. [69] compared to those obtained in the present experimental data. Higher surface tension provides more flow pattern stability resulting in a higher inertia force being required to achieve flow pattern transitions. Further, the high aspect ratio microchannel used here, when compared to the symmetric channels utilised in the work of Zhuang et al. [69], also anticipates different quantitative transitions when comparing our results.
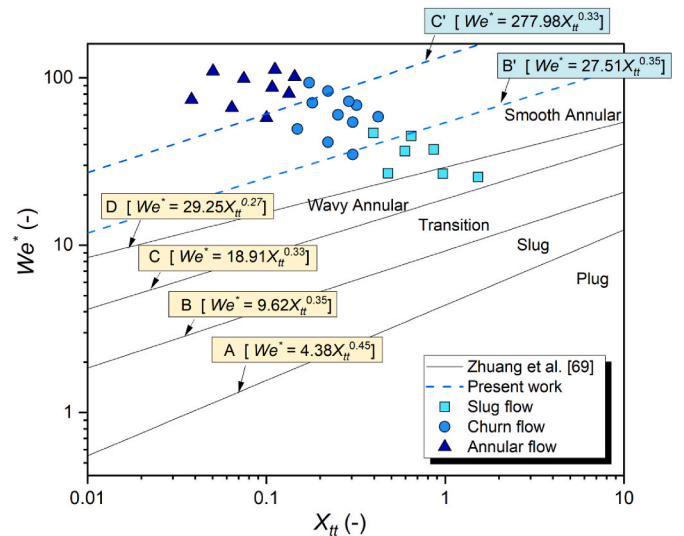


**Fig. 18.** The comparison of experimental data with a flow pattern map proposed by Zhuang et al. [69] with Martinelli parameter for turbulence case, $X_{tt}$, and modified Weber number, $We^*$, as the horizontal and vertical axis, respectively. The solid lines are the region transition lines of the proposed flow pattern map. The dashed lines show the fitted transition line of the present work for the slug-transition region and transition-wavy annular region.
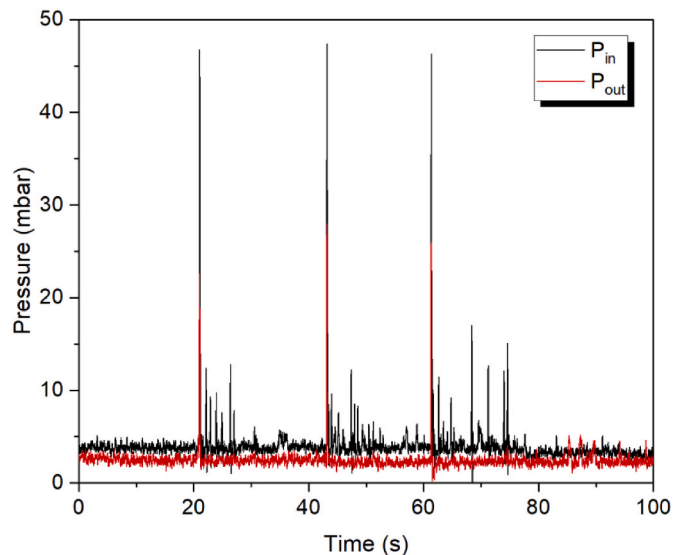


**Fig. 19.** Inlet and outlet pressure fluctuations ($G = 28$ kg m$^{-2}$ s$^{-1}$, equivalent to $Re = 56.8$, $q = 4.7$ kW m$^{-2}$ horizontal flow).

### 4.5. Flow instability analysis

Two-phase flow instability is characterised by pressure fluctuations seen during flow boiling. Fig. 19 depicts an example of the inlet and outlet pressure fluctuations for the case of $G = 28$ kg m$^{-2}$ s$^{-1}$ and $q = 4.7$ kW m$^{-2}$ and a horizontal flow configuration. The figure shows that there is a sudden pressure increase at a period of approximately 20 s, with the inlet pressure reaching around 45 mbar. After a high-pressure increase, it is followed by a lower pressure fluctuation that occurs several times before a new cycle starts.

A short period ($t = 60.9$–$61.9$ s) of pressure data is correlated with sequence images captured simultaneously by a high-speed video camera to understand the reason for the pressure fluctuation seen during flow boiling, as shown in Fig. 20. Initially, the pressure tends to be constant, below 5 mbar, and the snapshot on point A shows that the channel is
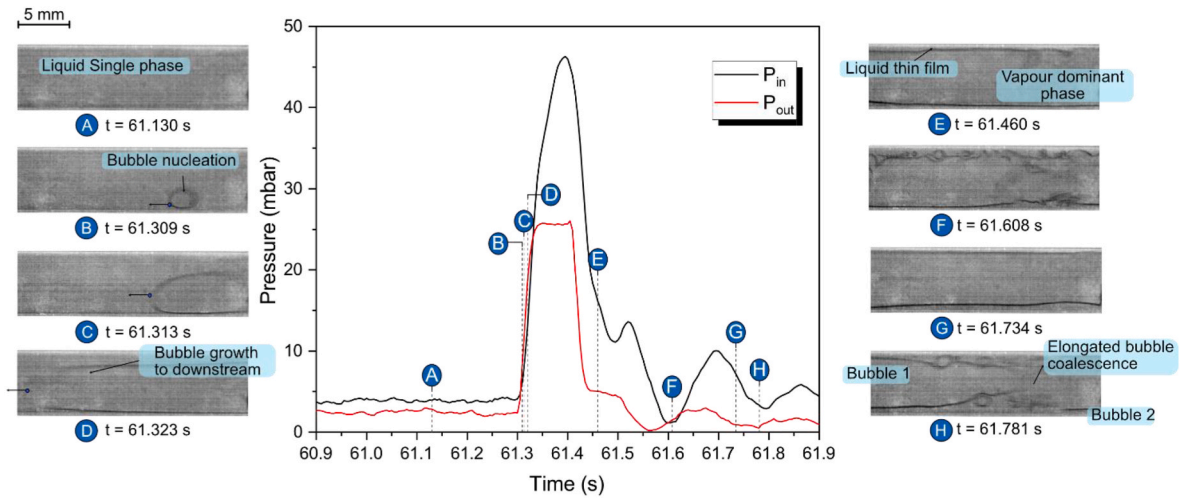
**Fig. 20.** Inlet and outlet pressure fluctuation for a period of 1 s, under horizontal flow configuration ($G = 28$ kg m$^{-2}$ s$^{-1}$, equivalent to $Re = 56.8$, $q = 4.7$ kW m$^{-2}$). The snapshot on the right and left sides of the main figure represents the phenomenon shown in a particular time pointed by the represented letters.

filled by liquid phase (single-phase flow). At $t = 61.309$ s, the bubble nucleation occurs in the channel. A sharp increase in both the inlet and outlet pressures is seen as the bubble grows rapidly. As suggested by Wang et al. [72], the rapid bubble growth triggers flow reversal due to the vapour bubble forces attempting to overcome the inertial force of the bulk liquid. This phenomenon can be observed at $t = 61.323$ s. When the vapour phase dominates within the microchannel, the pressure gradually drops. This is in accord with findings made by Kenning et al. [73], which suggested that the bubble growth initially causes a pressure increase followed by a gradual decrease when the bubble continues to expand and approach the end of the channel. At $t = 61.460$ s, the vapour dominant phase occupies the full observation area.

In addition, there are further slight pressure jumps during the flow boiling phenomenon, which can be associated with the bubble behaviour inside the microchannel. It is found that the mixing of the liquid and vapour phases, followed by a bubble nucleation event in the thin liquid film, as shown at $t = 61.608$ s (point F), also triggers a slight increase in the outlet pressure. This pressure increase is, however, not as high as that which was caused by the rapid bubble elongation growth. At $t = 61.781$ s, the coalescence between two elongated bubbles, initially

separated by the liquid phase, occurs in the outlet section of the microchannel. The bubble movement, followed by bubble growth due to evaporation, disturbs the stability of the liquid phase allowing two consecutive elongated bubbles to merge. This observation shows that the sequence of events also triggers a slight pressure jump.

Fig. 21 shows the flow boiling instability phenomenon in terms of temperature and pressure characteristics for the case of $G = 28$ kg m$^{-2}$ s$^{-1}$, $q = 4.7$ kW m$^{-2}$ under horizontal flow. The temperature fluctuation can be observed via IR thermography by capturing the evolution of wall temperature, $T_W$, during flow boiling. Here, as shown in the upper part of Fig. 21 a), the heated length was divided into ten regions. The average wall temperature of the region was obtained and plotted in Fig. 21 a) which depicts the channel wall temperature fluctuation versus time (s) during horizontal flow boiling for the case of low heat flux. The figure depicts a periodic fluctuation with a high amplitude and low frequency. During the low heat flux cases, the bubble grows from the nucleation site and experiences elongation until it fills the channel. The occurrence of intermittent liquid dominant and vapour dominant phases is the main reason for this periodic fluctuation. During the liquid-dominant phase, the wall temperature keeps increasing. As bubble nucleation occurs,
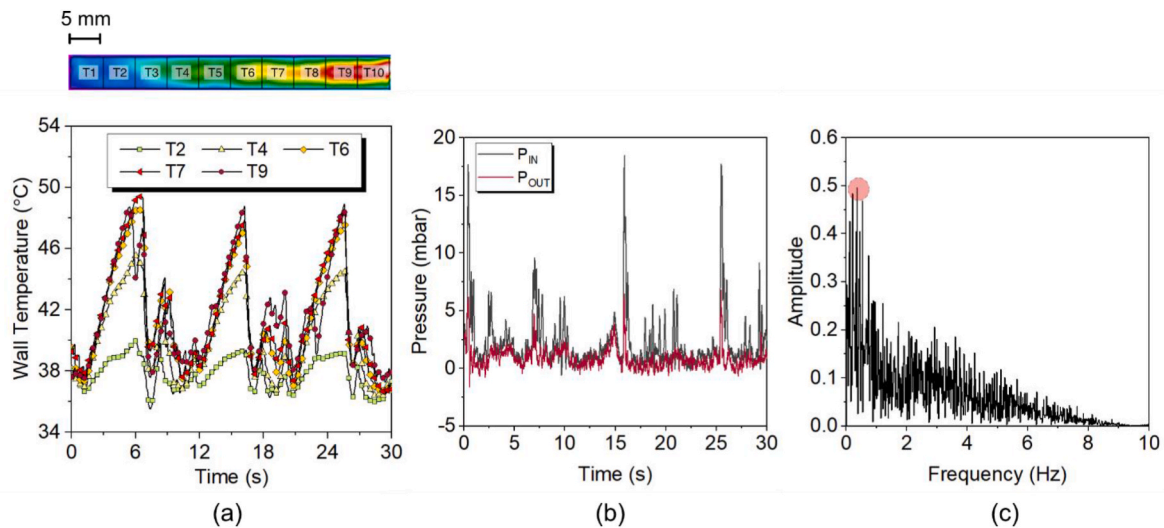


**Fig. 21.** Flow characteristics for horizontal microchannel flow boiling case at low heat flux ($G = 28$ kg m$^{-2}$ s$^{-1}$, equivalent to $Re = 56.8$, $q = 4.7$ kW m$^{-2}$). a) IR thermography of the microchannel wall temperature. The upper part illustrates the region of measurement. The lower part of the figure shows the average wall temperature, $T_W$ (°C), fluctuation versus time, $t$ (s). b) The fluctuation of inlet pressure, $P_{in}$ (mbar), and outlet pressure, $P_{out}$ (mbar), versus time. c) The result of FFT analysis of pressure drop ($P_{in}- P_{out}$).

there is a heat transfer improvement that leads to a temperature drop. Furthermore, Fig. 21 b) and Fig. 21 c) show the pressure characteristics during the flow boiling. In detail, Fig. 21 b) shows the pressure reading in the inlet and outlet section while Fig. 21 c) shows the result of the Fast Fourier Transform (FFT) analysis on the time-series data of pressure drop fluctuations. The high-pressure jump, which is similar to the trend of temperature fluctuation, represents the rapid bubble elongation in both the downstream and upstream directions. On the other hand, the low-pressure reading is due to the presence of a liquid dominant phase in the channel. The FFT result of the data reveals that the dominant frequency of this series is around 0.3 Hz, which is in accord with the cyclic temperature fluctuation.

As the heat flux is increased, more active nucleation sites appear within the channel. The presence of numerous small bubbles causes coalescence to occur more frequently, and it prevents the bubble from evolving into an elongated bubble. In addition, the increase of heat flux increases the vapour quality within the channel, so the intermittent flow, in the form of slug flow, is rarely observed. The transition of flow behaviour inside the channel directly influences both temperature and pressure fluctuations. Fig. 22 a) shows the channel wall temperature fluctuation for the case of $G = 28$ kg m$^{-2}$ s$^{-1}$ and $q = 14.5$ kW m$^{-2}$ at a horizontal flow configuration. The figure reveals that the temperature fluctuation has a higher frequency when compared to the case of low heat flux, which is presented in Fig. 21 a). In addition, the trend of temperature fluctuation for the measured regions of low heat flux shows a similar behaviour. On the other hand, the complex liquid-vapour interactions observed for high heat fluxes cause the local temperature fluctuation to differ for each region. This local fluctuation is affected by several phenomena, such as bubble nucleation, bubble coalescence, and liquid-vapour mixing.

Fig. 22 b) shows the inlet and outlet pressure fluctuation for the case of $G = 28$ kg m$^{-2}$ s$^{-1}$ and $q = 14.5$ kW m$^{-2}$ at a horizontal flow configuration. Similar to the temperature fluctuation seen in Fig. 22 a), the pressure behaviour undergoes intense fluctuations. The intense boiling and liquid-vapour interaction at a high heat flux produce local pressure fluctuation and become more dominant compared to the pressure fluctuation caused by the rapid bubble elongation process. This behaviour is described as high-frequency oscillation as suggested by previous researchers [38,72]. In addition, Fig. 22 b) shows the results of the FFT analysis from the pressure drop time-series data. The dominant frequency is found at around 4.3 Hz which is higher than the dominant frequency of the low heat flux case.

The observed flow instability during the microchannel flow boiling is strongly related to the bubble behaviour and the dominant flow pattern. The previous discussion shows that the bubble growth and rapid expansion along the channel trigger a very high amplitude oscillation with low frequency, i.e., long period. Hence, it is possible to conclude that the long period oscillation, caused by periodic bubble growth along the channel, is associated with intermittent flow, plug and slug flow. On the other hand, the short amplitude oscillation with high frequency, i.e., short period, is caused by complex liquid vapour interactions such as bubble nucleation (without bubble elongation process) in liquid slug or thin film and the liquid slug breakage. Those phenomena are mostly found in both churn and annular flow.

Fig. 23 shows the observed flow instability as a function of mass flux, $G$ (kg m$^{-2}$ s$^{-1}$), and heat flux, $q$ (kW m$^{-2}$). The figure reveals that under similar mass flux, the long period oscillation instability occurs at the low heat fluxes case. While as the mass flux increases, so does the heat flux needed to ensure the transition from long period oscillation instability to short period oscillation instability. It should be noted that Fig. 23 shows the data for the horizontal flow of the present work. Section 4.3 suggests
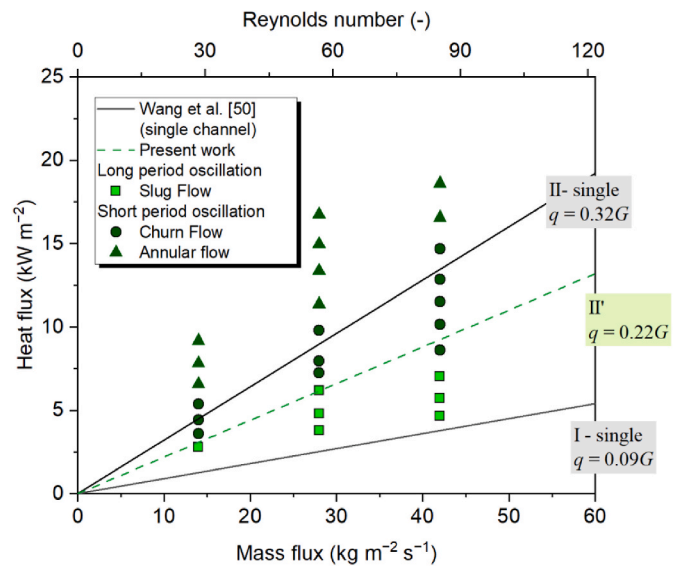


**Fig. 23.** Type of instability observed in the present work, long and short period oscillation, as a function of mass flux, $G$ (kg m$^{-2}$ s$^{-1}$), or Re number, and heat flux, $q$ (kW m$^{-2}$). Low period oscillation consists of slug flow while short period oscillation refers to churn and annular flow. Two solid lines represent the flow stability transition line proposed by Wang et al. [50]. Line I shows the transition from stable to long period oscillation unstable flow. Line II is the transition from long period oscillation to short period oscillation. The dashed line represents the transition line from long period oscillation to short period oscillation for the present work.
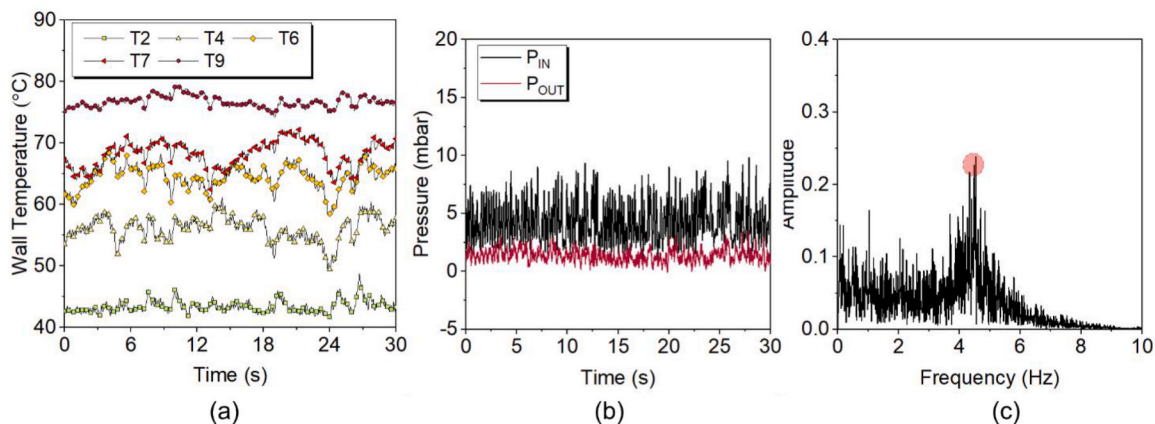


**Fig. 22.** Flow characteristics for horizontal microchannel flow boiling case at a high flux ($G = 28$ kg m$^{-2}$ s$^{-1}$, equivalent to $Re = 56.8$, $q = 14.5$ kW m$^{-2}$). a) The average wall temperature, $T_W$ (°C), fluctuation versus time, $t$ (s). b) The fluctuation of inlet pressure, $P_{in}$ (mbar), and outlet pressure, $P_{out}$ (mbar), versus time. c) The result of the FFT analysis of pressure drop ($P_{in - P_{out}}$).

that in the present work, there is no significant influence in the observed flow pattern for horizontal and vertical upward flow, so it is expected that the general trend of flow instability for horizontal and vertical upward flow remains the same. The flow instability trend in the present study was compared with that seen in the previous investigation. Wang et al. [50] investigated the flow boiling of water in both a single trapezoidal microchannel (a hydraulic diameter of 186 μm) and parallel microchannels. Based on the pressure and temperature fluctuation, three instability regimes of flow boiling were proposed. The study suggested the ratio of heat and mass flux as the transition line between the flow regime in a single channel, illustrated by the solid line in Fig. 23. The figure shows that the first transition line between the stable flow and oscillation flow can accurately predict the data in the present study. The proposed transition line for long period oscillation to short period oscillation ($q = 0.32G$) is also close to the transition line of the present study ($q = 0.22G$). The present study is focused on low mass fluxes, and it is found that all observed data are classified as unstable flow. Further experiments should be focused on the stable-unstable flow transition area towards achieving the goal of better thermal performance while maintaining a low mass flow rate in the micro cooling system.

## 5. Conclusion

The present experimental study investigated the bubble dynamics observed during flow boiling in a single, high aspect ratio microchannel equal to 10 with a hydraulic diameter of 909 μm. HFE7000 was chosen as the working fluid, and a transparent heating technique was utilised to provide uniform heating while maintaining transparency to enable a high-quality visualisation study. The conclusions of the present study are summarised below.

1. The bubble growth in the microchannel is divided into three stages. The transition from free bubble growth to partially confined growth occurs when the bubble equivalent diameters equal the channel depth. In addition, the bubble length-to-width aspect ratio of 1.1 is chosen as the onset of bubble elongation, representing the transition between the partial confinement and fully confined growth stages.
2. The effect of heat flux and mass flux, and buoyancy force due to channel orientation on bubble behaviour under the current experimental conditions is demonstrated. In vertical upward flow, the bubble experiences a slight decrease in the bubble length-to-width aspect ratio while it moves faster eased by buoyancy force. In terms of bubble typical shape, in horizontal flow, the bubble has a symmetrical shape, whilst a flat-shaped tail is found in vertical flow.
3. Although some differences are observed on the bubble dynamics behaviour when comparing the different orientations, these in turn do not influence significantly the flow pattern map reported. Therefore, further studies should be conducted to formulate the dominant parameters that influence the flow pattern development during microchannel flow boiling to be able to produce a pattern map that successfully predicts the flow pattern transition for this and other studies.
4. Two types of flow instabilities were observed based on the flow visualisation supported by the temperature and pressure characteristics. The first type of instability, high amplitude and long period oscillation, are observed in the slug flow due to the bubble rapid expansion along the channel. The second type of instability, short period oscillation, is associated with churn and annular flow due to the occurrence of multiple nucleation process and the breakage of liquid slug or liquid film. The transition between the instability is found as a function of the ratio of mass flux and heat flux which follows a correlation of $q = 0.22G$.

## Declaration of competing interest

The authors declare that they have no known competing financial interests or personal relationships that could have appeared to influence the work reported in this paper.

## Data availability

Data will be made available on request.

## Acknowledgements

## References

[1] J.R. Thome, A. Cioncolini, Flow Boiling in Microchannels, vol. 49, Elsevier Inc., 2017, https://doi.org/10.1016/bs.aiht.2017.06.001.

[2] G. Hetsroni, D. Klein, A. Mosyak, Z. Segal, E. Pogrebnyak, Convective boiling in parallel microchannels, Microscale Thermophys. Eng. 8 (4) (Jan. 2004) 403–421, https://doi.org/10.1080/10893950490516965.

[3] D.J. Chamund, L. Coulbeck, D.R. Newcombe, P.R. Waind, High power density IGBT module for high reliability applications, in: 2009 IEEE 6th International Power Electronics and Motion Control Conference, May 2009, pp. 274–280, https://doi.org/10.1109/IPEMC.2009.5157398. Wuhan.

[4] M.B. Bowers, I. Mudawar, High flux boiling in low flow rate, low pressure drop mini-channel and micro-channel heat sinks, Int. J. Heat Mass Tran. 37 (2) (Jan. 1994) 321–332, https://doi.org/10.1016/0017-9310(94)90103-1.

[5] I. Mudawar, Two-phase microchannel heat sinks: theory, applications, and limitations, J. Electron. Packag. 133 (4) (Dec. 2011), https://doi.org/10.1115/1.4005300, 041002.

[6] T.G. Karayiannis, M.M. Mahmoud, Flow boiling in microchannels: fundamentals and applications, Appl. Therm. Eng. 115 (2017) 1372–1397, https://doi.org/10.1016/j.applthermaleng.2016.08.063.

[7] K.R. Balasubramanian, R.J. Peter, R.A. Krishnan, Recent hypotheses on the parameters of microchannel flow boiling: a comprehensive overview, Microfluid. Nanofluidics 26 (10) (Oct. 2022) 80, https://doi.org/10.1007/s10404-022-02587-3.

[8] R. Ali, B. Palm, C. Martin-Callizo, M.H. Maqbool, Study of flow boiling characteristics of a microchannel using high speed visualization, J. Heat Tran. 135 (8) (Aug. 2013), https://doi.org/10.1115/1.4023879, 081501.

[9] L. Wojtan, R. Revellin, J.R. Thome, Investigation of saturated critical heat flux in a single, uniformly heated microchannel, Exp. Therm. Fluid Sci. 30 (8) (Aug. 2006) 765–774, https://doi.org/10.1016/j.expthermflusci.2006.03.006.

[10] B. Agostini, R. Revellin, J.R. Thome, Elongated bubbles in microchannels. Part I: experimental study and modeling of elongated bubble velocity, Int. J. Multiphas. Flow 34 (6) (Jun. 2008) 590–601, https://doi.org/10.1016/j.ijmultiphaseflow.2007.07.007.

[11] P.C. Lee, F.G. Tseng, C. Pan, Bubble dynamics in microchannels. Part I: single microchannel, Int. J. Heat Mass Tran. 47 (25) (2004) 5575–5589, Dec, https://doi.org/10.1016/J.IJHEATMASSTRANSFER.2004.02.031.

[12] B.R. Fu, M.S. Tsou, C. Pan, Boiling heat transfer and critical heat flux of ethanol–water mixtures flowing through a diverging microchannel with artificial cavities, Int. J. Heat Mass Tran. 55 (5–6) (2012) 1807–1814, Feb, https://doi.org/10.1016/J.IJHEATMASSTRANSFER.2011.11.051.

[13] Y. Wang, K. Sefiane, Effects of heat flux, vapour quality, channel hydraulic diameter on flow boiling heat transfer in variable aspect ratio micro-channels using transparent heating, Int. J. Heat Mass Tran. 55 (9–10) (2012) 2235–2243, Apr, https://doi.org/10.1016/j.ijheatmasstransfer.2012.01.044.

[14] O. Mokrani, B. Bourouga, C. Castelain, H. Peerhossaini, Fluid flow and convective heat transfer in flat microchannels, Int. J. Heat Mass Tran. 52 (5–6) (2009) 1337–1352, Feb, https://doi.org/10.1016/J.IJHEATMASSTRANSFER.2008.08.022.

[15] M. Vermaak, J. Potgieter, J. Dirker, M.A. Moghimi, P. Valluri, K. Sefiane, J. P. Meyer, Experimental and numerical investigation of micro/mini channel flow-boiling heat transfer with non-uniform circumferential heat fluxes at different rotational orientations, Int. J. Heat Mass Tran. 158 (2020), 119948, https://doi.org/10.1016/j.ijheatmasstransfer.2020.119948.

[16] R. Ajith Krishnan, K.R. Balasubramanian, S. Suresh, An experimental investigation on the effect of gravitational orientation on flow boiling performance in different channel sizes ranges from minichannels to microchannels, Heat Mass Tran. 56 (5) (May 2020) 1391–1420, https://doi.org/10.1007/s00231-019-02802-y.

[17] G. Bamorovat Abadi, C. Moon, K.C. Kim, Effect of gravity vector on flow boiling heat transfer, flow pattern map, and pressure drop of R245fa refrigerant in mini tubes, Int. J. Multiphas. Flow 83 (2016) 202–216, https://doi.org/10.1016/j.ijmultiphaseflow.2016.04.007.

[18] T. Layssac, S. Lips, R. Revellin, Effect of inclination on heat transfer coefficient during flow boiling in a mini-channel, Int. J. Heat Mass Tran. 132 (Apr. 2019) 508–518, https://doi.org/10.1016/j.ijheatmasstransfer.2018.12.001.

[19] M. Piasecka, K. Strąk, B. Maciejewska, Heat transfer characteristics during flow along horizontal and vertical minichannels, Int. J. Multiphas. Flow 137 (Apr. 2021) 103559, https://doi.org/10.1016/j.ijmultiphaseflow.2021.103559.

[20] G.K. Sinha, A. Srivastava, Experiments to compare the dynamics and thermal impact of single vapor bubble subjected to upward and downward flow boiling configurations, Exp. Heat Tran. 33 (6) (Sep. 2020) 487–509, https://doi.org/10.1080/08916152.2019.1662518.

[21] S.G. Kandlikar, P. Balasubramanian, An experimental study on the effect of gravitational orientation on flow boiling of water in 1054 × 197 μm parallel minichannels, J. Heat Tran. 127 (8) (2005) 820–829, https://doi.org/10.1115/1.1928911.

[22] H.Y. Zhang, D. Pinjala, Flow boiling heat transfer in microchannel heat sinks of different flow orientations, in: Advances in Electronic Packaging, Parts A, B, and C, Jan. 2005, pp. 51–58, https://doi.org/10.1115/IPACK2005-73041. San Francisco, California, USA.

[23] H.L.S.L. Leão, C.A. Chávez, F.J. Do Nascimento, G. Ribatski, An analysis of the effect of the footprint orientation on the thermal-hydraulic performance of a microchannels heat sink during flow boiling of R245fa, Appl. Therm. Eng. 90 (2015) 907–926, https://doi.org/10.1016/j.applthermaleng.2015.07.043.

[24] W. Li, Z. Chen, J. Li, K. Sheng, J. Zhu, Subcooled flow boiling on hydrophilic and super-hydrophilic surfaces in microchannel under different orientations, Int. J. Heat Mass Tran. 129 (Feb. 2019) 635–649, https://doi.org/10.1016/j.ijheatmasstransfer.2018.10.003.

[25] M. Vermaak, D. Orejon, J. Dirker, K. Sefiane, J.P. Meyer, Pressure and thermal characterisation of dynamic instabilities during flow boiling in micro/mini-channels at different azimuth orientations, Appl. Therm. Eng. 218 (Jan. 2023) 119292, https://doi.org/10.1016/j.applthermaleng.2022.119292.

[26] S. Saisorn, P. Wongpromma, S. Wongwises, The difference in flow pattern, heat transfer and pressure drop characteristics of mini-channel flow boiling in horizontal and vertical orientations, Int. J. Multiphas. Flow 101 (Apr. 2018) 97–112, https://doi.org/10.1016/j.ijmultiphaseflow.2018.01.005.

[27] A. Candan, B. Markal, O. Aydin, M. Avci, Saturated flow boiling characteristics in single rectangular minichannels: effect of aspect ratio, Exp. Heat Tran. 31 (6) (Nov. 2018) 531–551, https://doi.org/10.1080/08916152.2018.1463305.

[28] A.H. Al-Zaidi, M.M. Mahmoud, T.G. Karayiannis, Flow boiling of HFE-7100 in microchannels: experimental study and comparison with correlations, Int. J. Heat Mass Tran. 140 (Sep. 2019) 100–128, https://doi.org/10.1016/j.ijheatmasstransfer.2019.05.095.

[29] J.R. Thome, V. Dupont, A.M. Jacobi, Heat transfer model for evaporation in microchannels. Part I: presentation of the model, Int. J. Heat Mass Tran. 47 (14–16) (Jul. 2004) 3375–3385, https://doi.org/10.1016/j.ijheatmasstransfer.2004.01.006.

[30] G. Wang, L. Hao, P. Cheng, A four-zone model for saturated flow boiling in a microchannel of rectangular cross-section, Int. J. Heat Mass Tran. 53 (17–18) (2010) 3439–3448, https://doi.org/10.1016/j.ijheatmasstransfer.2010.04.001.

[31] A. Mukherjee, S.G. Kandlikar, Z.J. Edel, Numerical study of bubble growth and wall heat transfer during flow boiling in a microchannel, Int. J. Heat Mass Tran. 54 (15–16) (Jul. 2011) 3702–3718, https://doi.org/10.1016/J.IJHEATMASSTRANSFER.2011.01.030.

[32] E. Costa-Patry, J.R. Thome, Flow pattern-based flow boiling heat transfer model for microchannels, Int. J. Refrig. 36 (2) (Mar. 2013) 414–420, https://doi.org/10.1016/J.IJREFRIG.2012.12.006.

[33] S. Korniliou, C. Mackenzie-Dover, J.R.E. Christy, S. Harmand, A.J. Walton, K. Sefiane, Two-dimensional heat transfer coefficients with simultaneous flow visualisations during two-phase flow boiling in a PDMS microchannel, Appl. Therm. Eng. 130 (Feb. 2018) 624–636, https://doi.org/10.1016/j.applthermaleng.2017.11.003.

[34] K. Sakalkale, R. Majumdar, S.K. Saha, An investigation of two-phase flow regimes for microchannels based on void fraction, IEEE Trans. Compon. Packag. Manuf. Technol. 9 (11) (Nov. 2019) 2189–2199, https://doi.org/10.1109/TCPMT.2019.2918925.

[35] P. Valiorgue, S.N. Ritchey, J.A. Weibel, S.V. Garimella, Design of a non-intrusive electrical impedance-based void fraction sensor for microchannel two-phase flows, Meas. Sci. Technol. 25 (9) (2014), https://doi.org/10.1088/0957-0233/25/9/095301.

[36] G.K. Sinha, S. Mahimkar, A. Srivastava, Schlieren-based simultaneous mapping of bubble dynamics and temperature gradients in nucleate flow boiling regime: effect of flow rates and degree of subcooling, Exp. Therm. Fluid Sci. 104 (Jun. 2019) 238–257, https://doi.org/10.1016/j.expthermflusci.2019.02.018.

[37] H. Ide, R. Kimura, M. Kawaji, Optical measurement of void fraction and bubble size distributions in a microchannel, Heat Tran. Eng. 28 (8–9) (Aug. 2007) 713–719, https://doi.org/10.1080/01457630701328031.

[38] D. Bogojevic, K. Sefiane, G. Duursma, A.J. Walton, Bubble dynamics and flow boiling instabilities in microchannels, Int. J. Heat Mass Tran. 58 (1–2) (2013) 663–675, https://doi.org/10.1016/J.IJHEATMASSTRANSFER.2012.11.038.

[39] L. Yin, L. Jia, Confined bubble growth and heat transfer characteristics during flow boiling in microchannel, Int. J. Heat Mass Tran. 98 (2016) 114–123, https://doi.org/10.1016/j.ijheatmasstransfer.2016.02.063.

[40] S. Gedupudi, Y.Q. Zu, T.G. Karayiannis, D.B.R. Kenning, Y.Y. Yan, Confined bubble growth during flow boiling in a mini/micro-channel of rectangular cross-section Part I: experiments and 1-D modelling, Int. J. Therm. Sci. 50 (3) (Mar. 2011) 250–266, https://doi.org/10.1016/j.ijthermalsci.2010.09.001.

[41] J. Barber, D. Brutin, K. Sefiane, L. Tadrist, Bubble confinement in flow boiling of FC-72 in a 'rectangular' microchannel of high aspect ratio, Exp. Therm. Fluid Sci. 34 (8) (2010) 1375–1388, https://doi.org/10.1016/J.EXPTHERMFLUSCI.2010.06.011.

[42] M.K. Akbar, D.A. Plummer, S.M. Ghiaasiaan, On gas-liquid two-phase flow regimes in microchannels, Int. J. Multiphas. Flow 29 (5) (May 2003) 855–865, https://doi.org/10.1016/S0301-9322(03)00043-0.

[43] T. Harirchian, S.V. Garimella, A comprehensive flow regime map for microchannel flow boiling with quantitative transition criteria, Int. J. Heat Mass Tran. 53 (13–14) (Jun. 2010) 2694–2702, https://doi.org/10.1016/J.IJHEATMASSTRANSFER.2010.02.039.

[44] T. Harirchian, S.V. Garimella, Boiling heat transfer and flow regimes in microchannels—a comprehensive understanding, J. Electron. Packag. 133 (1) (Mar. 2011), https://doi.org/10.1115/1.4002721, 011001.

[45] M.M. Mahmoud, T.G. Karayiannis, Flow pattern transition models and correlations for flow boiling in mini-tubes, Exp. Therm. Fluid Sci. 70 (Jan. 2016) 270–282, https://doi.org/10.1016/J.EXPTHERMFLUSCI.2015.09.023.

[46] 3M Novec 7000 Engineered Fluid Datasheet (2018) accessed May 20, 2022, https://multimedia.3m.com/mws/media/121372O/3m-novec-7000-engineered-fluid-tds.pdf.

[47] P.A. Kew, K. Cornwell, Correlations for the prediction of boiling heat transfer in small-diameter channels, Appl. Therm. Eng. 17 (8–10) (Aug. 1997) 705–715, https://doi.org/10.1016/s1359-4311(96)00071-3.

[48] S.G. Kandlikar, W.J. Grande, Evolution of microchannel flow passages–thermohydraulic performance and fabrication technology, Heat Tran. Eng. 24 (1) (Jan. 2003) 3–17, https://doi.org/10.1080/01457630304040.

[49] Y. Wang, K. Sefiane, Single bubble geometry evolution in micro-scale space, Int. J. Therm. Sci. 67 (2013) 31–40, https://doi.org/10.1016/j.ijthermalsci.2012.11.011.

[50] G. Wang, P. Cheng, H. Wu, Unstable and stable flow boiling in parallel microchannels and in a single microchannel, Int. J. Heat Mass Tran. 50 (21–22) (2007) 4297–4310, Oct, https://doi.org/10.1016/j.ijheatmasstransfer.2007.01.033.

[51] S. Lee, V.S. Devahdhanush, I. Mudawar, Frequency analysis of pressure oscillations in large length-to-diameter two-phase micro-channel heat sinks, Int. J. Heat Mass Tran. 116 (Jan. 2018) 273–291, https://doi.org/10.1016/j.ijheatmasstransfer.2017.08.107.

[52] R.P. Madding, Emissivity Measurement and Temperature Correction Accuracy Considerations, in: Presented at the AeroSense '99, Mar. 1999, pp. 393–401, https://doi.org/10.1117/12.342307. Orlando, FL.

[53] S.-Y. Lee, J. Jang, S.T. Wereley, Effects of planar inlet plenums on the hydrodynamically developing flows in rectangular microchannels of complementary aspect ratios, Microfluid. Nanofluidics 5 (1) (Jul. 2008) 1–12, https://doi.org/10.1007/s10404-007-0179-y.

[54] Y. Wang, K. Sefiane, R. Bennacer, Investigation of boiling and bubble confinement in a high aspect ratio micro-channel, Appl. Therm. Eng. 31 (5) (2011) 610–618, https://doi.org/10.1016/j.applthermaleng.2010.05.024.

[55] R.J. Goldstein, K.-S. Lau, Laminar natural convection from a horizontal plate and the influence of plate-edge extensions, J. Fluid Mech. 129 (1) (Apr. 1983) 55, https://doi.org/10.1017/S0022112083000646.

[56] R.K. Shah, A.L. London, Rectangular Ducts," *Laminar Flow Forced Convection In Ducts*, 1978, pp. 196–222, https://doi.org/10.1016/B978-0-12-020051-1.50012-7.

[57] P.-S. Lee, S.V. Garimella, Saturated flow boiling heat transfer and pressure drop in silicon microchannel arrays, Int. J. Heat Mass Tran. 51 (3–4) (2008) 789–806, https://doi.org/10.1016/j.ijheatmasstransfer.2007.04.019.

[58] L. Yin, L. Jia, P. Guan, Bubble confinement and deformation during flow boiling in microchannel, Int. Commun. Heat Mass Tran. 70 (2016) 47–52, https://doi.org/10.1016/j.icheatmasstransfer.2015.11.004.

[59] Z.J. Edel, A. Mukherjee, Experimental investigation of vapor bubble growth during flow boiling in a microchannel, Int. J. Multiphas. Flow 37 (10) (Dec. 2011) 1257–1265, https://doi.org/10.1016/J.IJMULTIPHASEFLOW.2011.07.007.

[60] G.K. Sinha, A. Srivastava, Whole field measurements to quantify the thermal impact of single vapor bubble under nucleate flow boiling regime, Int. J. Heat Mass Tran. 157 (Aug. 2020) 119932, https://doi.org/10.1016/j.ijheatmasstransfer.2020.119932.

[61] G.K. Sinha, S. Narayan, A. Srivastava, Microlayer dynamics during the growth process of a single vapour bubble under subcooled flow boiling conditions, J. Fluid Mech. 931 (Jan. 2022) A23, https://doi.org/10.1017/jfm.2021.958.

[62] C.-C. Wang, W.-J. Chang, C.-H. Dai, Y.-T. Lin, K.-S. Yang, Effect of inclination on the convective boiling performance of a microchannel heat sink using HFE-7100, Exp. Therm. Fluid Sci. 36 (Jan. 2012) 143–148, https://doi.org/10.1016/j.expthermflusci.2011.09.006.

[63] D.J. Nicklin, Two-phase bubble flow, Chem. Eng. Sci. 17 (9) (Sep. 1962) 693–702, https://doi.org/10.1016/0009-2509(62)85027-1.

[64] P. Vasileiadou, K. Sefiane, T.G. Karayiannis, J.R.E. Christy, Flow boiling of ethanol/water binary mixture in a square mini-channel, Appl. Therm. Eng. 127 (Dec. 2017) 1617–1626, https://doi.org/10.1016/J.APPLTHERMALENG.2017.08.126.

[65] B. Markal, O. Aydin, M. Avci, Effect of aspect ratio on saturated flow boiling in microchannels, Int. J. Heat Mass Tran. 93 (Feb. 2016) 130–143, https://doi.org/10.1016/J.IJHEATMASSTRANSFER.2015.10.024.

[66] E. Costa-Patry, J. Olivier, J.R. Thome, Heat transfer charcacteristics in a copper micro-evaporator and flowpattern-based prediction method for flowboiling in microchannels, Frontiers in Heat and Mass Transfer 3 (1) (2012), https://doi.org/10.5098/hmt.v3.1.3002.

[67] L. Zhao, K.S. Rezkallah, Gas-liquid flow patterns at microgravity conditions, Int. J. Multiphas. Flow 19 (5) (Oct. 1993) 751–763, https://doi.org/10.1016/0301-9322(93)90041-R.

[68] R. Revellin, J.R. Thome, A new type of diabatic flow pattern map for boiling heat transfer in microchannels, J. Micromech. Microeng. 17 (4) (2007) 788–796, https://doi.org/10.1088/0960-1317/17/4/016.

[69] X. Zhuang, M. Gong, G. Chen, X. Zou, J. Shen, Two-phase flow pattern map for R170 in a horizontal smooth tube, Int. J. Heat Mass Tran. 102 (2016) 1141–1149, https://doi.org/10.1016/j.ijheatmasstransfer.2016.06.094.

[70] K.S. Rezkallah, Weber number based flow-pattern maps for liquid-gas flows at microgravity, Int. J. Multiphas. Flow 22 (6) (Nov. 1996) 1265–1270, https://doi.org/10.1016/0301-9322(96)00047-X.

[71] H.M. Soliman, The mist-annular transition during condensation and its influence on the heat transfer mechanism, Int. J. Multiphas. Flow 12 (2) (Mar. 1986) 277–288, https://doi.org/10.1016/0301-9322(86)90030-3.

[72] Y. Wang, K. Sefiane, Z.G. Wang, S. Harmand, Analysis of two-phase pressure drop fluctuations during micro-channel flow boiling, Int. J. Heat Mass Tran. 70 (Mar. 2014) 353–362, https://doi.org/10.1016/j.ijheatmasstransfer.2013.11.012.

[73] D.B.R. Kenning, D.S. Wen, K.S. Das, S.K. Wilson, Confined growth of a vapour bubble in a capillary tube at initially uniform superheat: experiments and modelling, Int. J. Heat Mass Tran. 49 (23–24) (Nov. 2006) 4653–4671, https://doi.org/10.1016/j.ijheatmasstransfer.2006.04.010.